Dear Jorge D'Elia,

Based on the comments received, the evaluation returned, and the recommendation of Associate Editor, Professor Ye Zhou has recommended your manuscript be accepted for publication in the Journal of Fluids Engineering. I am in agreement with this recommendation, and am happy to inform you that your paper will appear in a future issue of the Journal. Please read and follow these instructions, because your paper will not go into print until you've prepare the paper to comply with production requirements!

The detailed comments of the reviewers are available for your further consideration. Please log in to the web site to see these comments, and please update the paper according to any final recommendations provided.

Use the following check-list to avoid common problems with your final files:

1) Follow the ASME instructions exactly as described, your submission will be returned to you and won't go into production until they are correct. Full instructions are here:
http://journaltool.asme.org/Help/AuthorHelp/WebHelp/JournalsHelp.htm

a.   Abstract Length: no more than 400 words for a research paper, 100 for technical brief.
b.   Format citations and references correctly. Use Chicago style referencing.
c.   Equations numbered and centered correctly.
d.   The contrast of figures and text no smaller than 6pt.
e.   Figures format: must be .eps or .tif.
f.   Tables longer than 6 rows should be treated as figures.
g.   Acknowledgments section, which should be succinct.

2) Color figures for the print version incur additional charges when put into print (these can't be waived).

3)Complete and submit the ASME copyright form 1903 to journalcopyright@asme.org . If you have trouble locating the "add 1903 form" link then please email directly to the copyright office and they will email the link to you.

4)This is also an excellent opportunity to update your paper citations. Please be sure to cite the journal properly (ASME J. Fluids Eng.).

LaTeX users have special requirements, but a template is available at:
http://iel.ucdavis.edu/code/ASME/journal-1.0.html.

Sincerely,
Malcolm J. Andrews
Editor, Journal of Fluids Engineering

Galerkin boundary elements for a computation of the surface tractions in exterior Stokes flows

Jorge D'Elía[*]

Senior Researcher
CIMEC (UNL-CONICET)
Predio Conicet-Santa Fe, Colectora RN 168
El Pozo, Santa Fe (3000), Argentina
Email: jdelia@intec.unl.edu.ar

Laura Battaglia[* †]

Graduate Researcher
CIMEC (UNL-CONICET)
GIMNI, UTN-FRSF
Lavaisse 610, Santa Fe (3000), Argentina
Email: lbattaglia@santafe-conicet.gob.ar

Alberto Cardona, Mario Storti[*]
Professors, Senior Researchers
CIMEC (UNL-CONICET)
Email: acardona@intec.unl.edu.ar, mstorti@intec.unl.edu.ar
Gustavo Ríos Rodríguez
Graduate Researcher
Email: gusadrr@santafe-conicet.gov.ar

In the computation of a three–dimensional steady creeping flow around a rigid body, the total body force and torque are well predicted using a Boundary Integral Equation (BIE) with a single concentrated pair Stokeslet- rotlet located at an interior point of the body. However, the distribution of surface tractions are seldom considered. Then, a completed indirect velocity BIE of Fredholm type and second-kind is employed for the computation of the pointwise tractions, and it is numerically solved by using either collocation or Galerkin weighting procedures over flat triangles. In the Galerkin case, a full numerical quadrature is proposed in order to handle the weak singularity of the tensor kernels, which is an extension for fluid engineering of a general framework (Taylor, D. J., 2003, "Accurate and efficient numerical integration of weakly singulars integrals in Galerkin EFIE solutions", IEEE Trans. on Antennas and Propag., 51(7):1630-1637). Several numerical simulations of steady creeping flow around closed bodies are presented, where results compare well with semi-analytical and finite-element solutions, showing the ability of the method for obtaining the viscous drag and capturing the singular behavior of the surface tractions close to edges and corners. Also, deliberately intricate geometries are considered.

---

[*]Centro de Investigación de Métodos Computacionales (CIMEC), Universidad Nacional del Litoral (UNL), Consejo Nacional de Investigaciones Científicas y Técnicas (CONICET).

[†]Grupo de Investigación en Métodos Numéricos en Ingeniería (GIMNI), Facultad Regional Santa Fe (FRSF), Universidad Tecnológica Nacional (UTN).

1

1 Introduction

Numerical simulations of steady creeping flows, or Stokes flows, around closed rigid bodies can be of interest in fluid engineering and biomedical engineering problems. Two numerical methods frequently used are the boundary element method (BEM) and the finite element method (FEM) [1].

In particular, BEM is based on the formulation of a boundary value problem (BVP) of elliptic type as a boundary integral equation (BIE) [2]. In general, BEM can be more suitable for problems involving a low ratio of boundary surface to volume, high accurate boundary stresses, or with incompressible materials, while FEM can be well suited in the opposite cases. Besides, mixed BEM-FEM analysis are commonly used [1]. Among the most relevant differences between BEM and FEM, the following stand out [1, 2]:

1. Geometry discretization: (i) the mesh generation for BEM is simpler than for FEM in three-dimensional (3D) spatial domains with intricate geometries, since in the former only a surface mesh of the domain must be performed instead of a full volume mesh; (ii) an unbounded domain is immediate to handle with BEM, while FEM requires a volume mesh on an unbounded domain; (iii) identifying connectivity errors in volume meshes can be more difficult than in surface meshes;

2. Material properties: (i) the BEM approach generally uses the Green function in an infinite domain; therefore, it is only applicable to problems that can be approximated by linear differential operators; (ii) in homogeneous, isotropic, linearized 3D elasticity, the fundamental solution and mapping properties of the boundary integral operators remain unchanged in the incompressible limit, i.e. in the passage from the Lamé-Navier equations to the Stokes equations, while the function spaces for FEM change in the incompressible limit, due to the appearance of the incompressibility constraint $\text{div}(\mathbf{u}) = 0$ in the domain, which is accounted for exactly by the Kelvin tensor. As a consequence, a BEM for incompressible materials (solid or viscous fluids) does not exhibit the so-called locking effect, a well-known problem in FEM;

3. Numerical methods: (i) the matrix system in BEM is dense (fully populated) and, in general, non-symmetric, while the FEM system matrix is much larger, although sparse; (ii) the linear system obtained with a second kind BIE has, in general, a better condition number than that obtained with FEM.

The standard discretization procedure of a BIE consists of three parts [3]: the tessellation of the boundary surfaces, the approximation of the solution field with a linear combination of polynomial basis functions, and the minimization of the error of the approximate solution with respect to some weighting functions. A simple tessellation of the boundary surface can be performed with flat simplex triangles, or elements, where their vertices are also the nodes of the boundary mesh. The basis functions can be defined either on the elements, the nodes or the edges of the boundary mesh. In order to find an approximate solution, the residue is minimized with respect to a set of linearly independent weighting functions, using e.g. point collocation or Galerkin weighting techniques.

A point collocation technique minimizes the residue at a discrete set of points that, in the case of using constant basis functions, typically consists of the centroids of the elements. Single surface integrations are used generating a non-symmetric system of algebraic equations. Several schemes for fast integration have been developed for collocation techniques. For instance, analytic expressions for surface potentials using isoparametric piecewise linear shape functions over flat triangles were developed in [4], whereas non-linear transformations for nearly singular integrals over planar triangles were used in collocation techniques in [5].

2

Closed forms derived from a side local frame strategy are also commonly employed [6], where the surface integral over an element is replaced by its closed contour integration, and a side local frame is used for each side contribution, with applications, e.g. in free surface flows [7], seakeeping [8] and exterior flows [9].

In the Galerkin weighting technique, the residue is minimized by averaging over the boundary surface, with weighting functions chosen to be identical to the basis functions. This leads to a symmetric system of linear equations, at the expense of performing double surface integrations. Examples of weighted residual techniques in a BIE include the variational BEM [10], the symmetric BEM, and the symmetric Galerkin BEM [11–13].

Several boundary integral equations are of Fredholm type of first or second kind, and they are obtained either through direct or indirect integral formulations [2]. On the one hand, a direct BIE uses as starting point the weighted residual expression [2]. All derivatives acting on the unknown field variables are passed by integration by parts to the weight functions. When the selected weight function is a fundamental solution of the differential equation, an equivalent BIE formulation of the BVP is obtained. It should be noted that the actual physical quantities of interest are used from the outset in this formulation. On the other hand, an indirect BIE uses as a starting point the potentials produced by surface layers of (fictitious) singularities [2]. The surface singularity layers generate the physical fields of interest, and they are associated with the so-called influence functions. The surface singularity layers are distributed on the boundary and their intensities have to be determined such that the integrated response is equal to the prescribed boundary data. Next, the surface singularity layers are inserted into the associated potentials, giving the solution fields of the boundary value problem. Therefore, in this formulation, the physical variables of interest in the boundary value problem are not the solution of the BIE, but they are obtained afterwards by post-treatment. From a mathematical point of view, the unknowns in the direct BIE are the traces of the solution of the underlying partial differential equation and its normal derivative, while the unknowns in the indirect BIE

are the jumps of the traces across the boundary of the Cauchy data of both the interior and the exterior BVP [2]. From a practical point of view, the difference between both methods is in the source points: in the direct method, the free point x is the source point, while in the indirect method the integration points y are the source points.

Indirect formulations for creeping (or Stokes) flows, with Reynolds numbers Re < 1, are commonly related to hydrodynamic single- and double-layer potentials [14–16]. Examples of creeping flows in fluid engineering and biomedical engineering include multilevel BEM for steady Stokes flows in irregular domains [17]; low Reynolds number flows in spiral microchannels used in DNA identifying lab-on-a-chip devices [18]; creeping flow regime in oscillatory-flow mixers with flexible chambers [19], micro-electro-mechanical systems (MEMS) [20,21], and laminar flow in compact heat exchangers and microcoolers in electronics packaging [22].

Ingber and Mammoli [23] have analyzed the case of BIE for creeping flows, and showed comparisons among three different formulations:

(i) Direct velocity BIE (DV-BIE) a Fredholm BIE of first kind for the velocity is proposed, where the boundary conditions are given in terms of velocity components;

(ii) Completed indirect velocity BIE (CIV-BIE) [24] (or completed double-layer (CDL-BIE) [25]): it fixes the deficient range of the integral operator of a double-layer velocity potential, obtaining a well posed problem and giving the total force and torque acting on the rigid body;

(iii) Uncompleted direct traction BIE (UDT-BIE) [26, 27]: an hypersingular BIE for the traction is developed that is calculated using a regularization technique, with an exterior collocation scheme to constrain out the six rigid body eigenmodes.

Furthermore, Keaveny and Shelley [28] employed a completed indirect traction BIE (CIT-BIE). Hebeker [29] and Gonzalez [30] proposed related formulations with smooth surfaces in simple geometries, and were able to determine the total force and torque acting on the rigid body, although the pointwise value of surface traction was not directly

accessible, nor a Galerkin weighting had been employed.

In the present work, a completed indirect velocity BIE (CIV-BIE) of Fredholm type and second kind is employed to determine the pointwise value of traction in steady creeping flows around 3D rigid bodies with sharp corners and edges. The BIE is numerically solved by using either collocation (BEM) or Galerkin weighting procedures (GBEM). In the Galerkin case, a systematic full numerical quadrature is employed in order to handle three types of surface integrals with a weak singularity that arise when calculating the interaction among all the elements of the boundary mesh, which is an extension for fluid engineering of a particular framework proposed by Taylor [31] for the Helmholtz equation. Gauss-Legendre quadrature formulas, and flat simplex triangles are used in all cases. For easiness of presentation, the formulation for an isolated rigid body and Newtonian incompressible viscous fluid is developed. The present approach is applied to closed surfaces, and uses either collocation with constant shape functions or Galerkin weighting with linear shape functions. Numerical examples display calculation of the steady creeping flow around several closed bodies, including, as validation cases, the unit sphere, the unit cube and the unit torus, other bodies with edges and corners, and some deliberately intricate geometries. Results are compared to analytical solutions for several inflow conditions in the sphere case. In the cube case, comparisons are made with semi-analytical solutions proposed by Mustakis-Kim [32] for several inflow patterns. In other cases, the results are validated using finite element analysis. Solution convergence under mesh refinement and numerical stability under mesh perturbations with respect to a regular mesh are determined and compared for all formulations.

2 Boundary integral equation

In this section, the completed indirect velocity BIE (termed as "completed double-layer BIE" by [25]) is summarized in the Hebeker [29] version, that employs double- and single-layer surface densities distributed on the body surface.

2.1 Stokes equations for an exterior and steady creeping flow around a fixed body

When a steady creeping flow passes around a fixed body of arbitrary shape, the perturbed fluid velocity $v_i = v_i(\boldsymbol{x})$, for $i = 1, 2, 3$, and pressure $p = p(\boldsymbol{x})$ fields satisfy the Stokes equations [14]

$$\mu \frac{\partial^2 v_i}{\partial x_j \partial x_j} = \frac{\partial p}{\partial x_i}$$
$$\frac{\partial v_i}{\partial x_i} = 0 \tag{1}$$

for all points $\boldsymbol{x} = (x_1, x_2, x_3)$ in the unbounded exterior domain Ω^e to the body surface A, where μ is the dynamic fluid viscosity. The perturbed velocity $v_i(\boldsymbol{x})$ satisfies the no-slip boundary condition on the body surface A given by

$$v_i(\boldsymbol{x}) + u_i(\boldsymbol{x}) = 0 \qquad \text{for all } \boldsymbol{x} \in A, \tag{2}$$

where $u_i(\boldsymbol{x})$ is the unperturbed velocity, and the asymptotic behavior at infinity

$$\begin{aligned} v_i(\boldsymbol{x}) &= O(1/R) \\ p(\boldsymbol{x}) &= O(1/R^2) \end{aligned} \qquad \text{as } R \to \infty \tag{3}$$

where $R = \|\boldsymbol{x}\|_2$ is the Euclidean distance from the origin $O(x, y, z)$.

2.2 Potential of a double-layer surface density

The potential due to a Double-Layer (DL) surface density $\boldsymbol{\psi}$ is defined as [14]

$$w_i^{\text{DL}}(\boldsymbol{x}; \boldsymbol{\psi}) = \int_A \tilde{K}_{ij}(\boldsymbol{x}, \boldsymbol{y}) \psi_j(\boldsymbol{y}) \, dA_{\boldsymbol{y}}$$
$$\text{with} \quad \tilde{K}_{ij}(\boldsymbol{x}, \boldsymbol{y}) = -\frac{3}{4\pi} \frac{r_i r_j r_k}{r^5} n_k(\boldsymbol{y}) \tag{4}$$

where $dA_{\boldsymbol{y}} = dA(\boldsymbol{y})$ is the differential of area, $\boldsymbol{y} = (y_1, y_2, y_3)$ is the source point, $\boldsymbol{r} = \boldsymbol{x} - \boldsymbol{y} = (r_1, r_2, r_3)$ is the relative position, and $r = \|\boldsymbol{r}\|_2$, while $\boldsymbol{n}(\boldsymbol{y})$ is the external unit normal to the surface A at $\boldsymbol{y}$.

4

2.3 Potential of a single-layer surface density

The potential due to a Single-Layer (SL) surface density ϕ is defined as [14]

$$w_i^{\text{SL}}(\boldsymbol{x};\boldsymbol{\phi}) = \int_A \hat{S}_{ij}(\boldsymbol{x},\boldsymbol{y})\phi_j(\boldsymbol{y})\,\mathrm{d}A_{\boldsymbol{y}}$$

$$\text{where} \quad \hat{S}_{ij}(\boldsymbol{x},\boldsymbol{y}) = -\frac{1}{8\pi\mu}\left[\frac{\delta_{ij}}{r} + \frac{r_i r_j}{r^3}\right] \tag{5}$$

2.4 Double and single layer potentials in exterior flows

It is well-known that the velocity $w_i^{\text{DL}}(\boldsymbol{x};\boldsymbol{\psi})$ and pressure $p^{\text{DL}}(\boldsymbol{x};\boldsymbol{\psi})$ fields due to a DL potential generated by a surface density $\boldsymbol{\psi}$ decrease as

$$\begin{aligned} w_i^{\text{DL}}(\boldsymbol{x};\boldsymbol{\psi}) &= O(1/R^2) \\ p^{\text{DL}}(\boldsymbol{x};\boldsymbol{\psi}) &= O(1/R^3) \end{aligned} \tag{6}$$

as $R \to \infty$, and cannot exert neither a net force nor a net torque on the surface A. Since a DL potential produced by a density $\boldsymbol{\psi}$ alone cannot reproduce an arbitrary regular Stokes flow in the exterior domain Ω^e, Odqvist added an ad-hoc combination of six SL potentials produced by density layers $\boldsymbol{\phi}_i$ to fix this shortcoming [14, 24]. The densities of these SL potentials are the eigenfunctions of the adjoint integral operator of the DL potential. However, in general they are not explicitly known [24].

2.5 Completed double-layer BIE

The "completed double-layer boundary integral equation method" [25] completes the deficient range of the DL potential without recourse to the eigenfunctions of its adjoint integral operator. It can be regarded as a compound DL representation for external flows and it is written as ([33], Sec. 4.7, p. 127)

$$v_i(\boldsymbol{x}) = w_i^{\text{DL}}(\boldsymbol{x};\boldsymbol{\psi}) + \mathcal{V}_i(\boldsymbol{x}) \tag{7}$$

where $\mathcal{V}_i$ is a supplementary flow that is required to be regular in the exterior of the body surface A and to produce a finite force and torque on A.

2.5.1 The Hebeker alternative

Hebeker ([33], Sec. 4.7, p. 127, and [29] , Sec. II, p. 277), identified the supplementary flow $\mathcal{V}$ with the one due to a SL potential, whose density ϕ is proportional to the density $\boldsymbol{\psi}$ of the DL potential one, i.e.

$$\boldsymbol{\phi}(\boldsymbol{x}) = \chi_H\,\boldsymbol{\psi}(\boldsymbol{x}) \tag{8}$$

where χ_H is an arbitrary positive free parameter. This "Hebeker coupling parameter" takes into account that the physical units of both surface densities are different, because $\boldsymbol{\phi}$ is a force surface density, or pressure, while $\boldsymbol{\psi}$ is a perturbation velocity surface density. The Hebeker alternative can be written as the BIE (see appendices A-B)

$$\int_A \tilde{K}_{ij}\,\psi_j(\mathbf{x})\,\mathrm{d}A_{\mathbf{y}} - \int_A \tilde{H}_{ij}\,\psi_j(\mathbf{y})\,\mathrm{d}A_{\mathbf{y}} = u_i(\mathbf{x}) \tag{9}$$

for all $\boldsymbol{x} \in A$, where

$$\tilde{H}_{ij} = \tilde{K}_{ij} + \chi_H \tilde{S}_{ij} \tag{10}$$

with $\tilde{K}_{ij}$ and $\tilde{S}_{ij}$ given by Eqs. (4-5), respectively. Equation (9) is a boundary integral equation for $\boldsymbol{\psi}(\boldsymbol{x})$ for all $\boldsymbol{x} \in A$ and, using matrix notation, is rewritten as

$$\boldsymbol{g}(\boldsymbol{x}) = \boldsymbol{u}(\boldsymbol{x}) \quad \text{for all } \boldsymbol{x} \in A \tag{11}$$

which is a BIE of Fredholm type and second kind with source term $\boldsymbol{u}(\boldsymbol{x})$, whereas

$$\boldsymbol{g}(\boldsymbol{x}) = \int_A \left[\tilde{\boldsymbol{K}}\boldsymbol{\psi}(\boldsymbol{x}) - \tilde{\boldsymbol{H}}\boldsymbol{\psi}(\boldsymbol{y})\right]\,\mathrm{d}A_{\boldsymbol{y}} \quad \text{for all } \boldsymbol{x} \in A \tag{12}$$

is a boundary integral operator with kernels $\tilde{\boldsymbol{K}}(\boldsymbol{x},\boldsymbol{y})$ and $\tilde{\boldsymbol{H}}(\boldsymbol{x},\boldsymbol{y})$. These kernels couple the double-layer surface density $\boldsymbol{\psi}$ at the integration point $\boldsymbol{y}$ and at the field point $\boldsymbol{x}$. In the Hebeker work [29], an analysis of the influence of the choice of χ_H in the numerical solution was performed, using collocation with piecewise bilinear shape functions on smooth 3D surfaces, showing little sensitivity around the unit value. Therefore, a unit value $\chi_H = 1$ is used in all the examples shown in this work.

2.6 Forces and surface traction field computation

The total body force $\boldsymbol{F} = (F_1, F_2, F_3)$ and torque $\boldsymbol{C} = (C_1, C_2, C_3)$ with respect to the origin $O(x,y,z)$ of the Cartesian coordinate system, are computed by the surface integrals [24]

$$\boldsymbol{F} = \int_A \boldsymbol{\phi}(\boldsymbol{y}) \, \mathrm{d}A_{\boldsymbol{y}} \quad \text{and} \quad \boldsymbol{C} = \int_A [\boldsymbol{y} \times \boldsymbol{\phi}(\boldsymbol{y})] \, \mathrm{d}A_{\boldsymbol{y}}$$
(13)

The traction field on the body surface is the superposition of the tractions caused by the single- and double-layer potentials. The direct value of these tractions (on the body surface) can be obtained by computing a boundary integral that is weakly singular in the first case, and hypersingular in the second [30]. Since this work is mainly oriented to a numerical scheme for the first case, then, as a first approximation, only the contribution of the single-layer potential is computed. With this simplification, the traction field $t_i(\boldsymbol{x}) = \sigma_{ij}(\boldsymbol{x}) n_j(\boldsymbol{x})$ at the field point $\boldsymbol{x}$, where $\sigma_{ij}(\boldsymbol{x})$ is the stress tensor, is obtained using (e.g. see [16], Sec. 3.2, Eq. 24, p. 58),

$$t_i(\boldsymbol{x})_{(e)} = -\frac{1}{2}\phi_i(\boldsymbol{x}) - \frac{3}{4\pi} \int_A \tilde{K}_{ji}(\boldsymbol{y}, \boldsymbol{x}) \phi_j(\boldsymbol{y}) \, \mathrm{d}A_{\boldsymbol{y}}$$
(14)

for $\boldsymbol{x} \in A$, where $\tilde{K}_{ji}(\boldsymbol{y}, \boldsymbol{x})$ is the transposed kernel from Eq. (4), and $\phi_j(\boldsymbol{y})$ is the single-layer surface density given in Eq. (8). It should be noted that Eq. (14) assumes that the unit normal $\boldsymbol{n}(\boldsymbol{x})$ is well defined at the field point $\boldsymbol{x}$. This restriction precludes the use of this equation for the computation of the traction field at points with geometric discontinuities, such as nodes, edges or vertices of the polyhedral surface mesh, at least in a classical sense. This shortcoming is simply avoided by computing tractions at the element centroids. Nondimensional body force $\hat{F}$, body torque $\hat{C}$ and surface traction τ are defined as

$$\hat{F}_i = \frac{F_i}{\mu U_\infty L} \quad \text{and} \quad \hat{F} = \frac{F}{\mu U_\infty L}$$

$$\hat{C}_i = \frac{C_i}{\mu U_\infty L^2} \quad \text{and} \quad \hat{C} = \frac{C}{\mu U_\infty L^2}$$

$$\tau_i(\boldsymbol{x}) = \frac{t_i(\boldsymbol{x})}{\mu U_\infty L^{-1}} \quad \text{and} \quad \tau(\boldsymbol{x}) = \frac{t(\boldsymbol{x})}{\mu U_\infty L^{-1}}$$
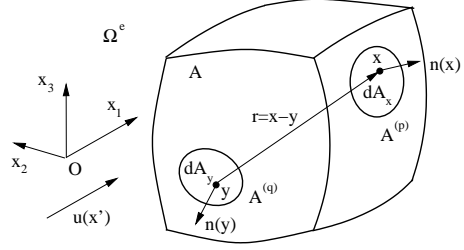(15)

Fig. 1. Sketch of a closed and piecewise smooth surface A with an exterior flow domain Ω^e: the field point $\boldsymbol{x}$, the source point $\boldsymbol{y}$, the relative position $\boldsymbol{r} = \boldsymbol{x} - \boldsymbol{y}$, the unit normals $\boldsymbol{n}(\boldsymbol{x}), \boldsymbol{n}(\boldsymbol{y})$, and the differential areas $\mathrm{d}A_{\boldsymbol{x}}, \mathrm{d}A_{\boldsymbol{y}}$

where U_∞ is the (unperturbed) speed, L is a typical length, $F = \|\boldsymbol{F}\|_2$, $C = \|\boldsymbol{C}\|_2$ and $t = \|\boldsymbol{t}\|_2$. The subindex $i = 1, 2, 3$ indicates the corresponding x_i Cartesian component.

3 Numerical formulations

Two numerical formulations are considered for solving the integral boundary equation given by Eq. (9). First, a collocation technique is employed and, then, a GBEM is used [2, 14]. Numerical results were found using both methods. In GBEM, a full numerical quadrature on the four coordinates over triangles is applied, in order to handle the weak singularity of the kernels. These techniques use a doubly nested loop over the elements $p, q = 1, 2, ..., E$, where the points $\boldsymbol{x}$ and $\boldsymbol{y}$ are related to the elements p, q, respectively, see Fig. 1. Element and nodal values are denoted with supra and sub indexes, respectively. The implementation details are given to Appendix C.

4 Numerical examples

The creeping flows around rigid bodies are considered, whose centers are placed at the origin of coordinates. First, a sphere, a torus, and a rigid cube with flat sides are considered for validation purposes. In the sphere case, results are compared to analytical solutions for several inflow conditions. In the torus case, results are compared to a semi-analytical solution developed by Amarakoon *et al.* [34]. In the cube case, comparisons are made with semi-analytical solutions proposed by Mustakis and Kim [32], for several flow patterns in order to check the traction laws close to the edges and vertices. The results for the paral-

6

Table 1. Number of nodes N and number of elements E for each mesh. Meshes 1-11 are structured meshes for the sphere and cube cases, while mesh 12 is an unstructured mesh built for the cube

Mesh	1	2	3	4	5	6	7	8	9	10	11	12
N	218	386	602	866	1178	1538	2402	3458	4706	5402	6938	674
E	432	768	1200	1728	2352	3072	4800	6912	9408	10800	13072	1344

Table 2. Steady creeping flow around a sphere of radius $\mathcal{R}$. Analytical expressions for the viscous force and torque, with respect to the center of the sphere, for three incoming flows ([33])

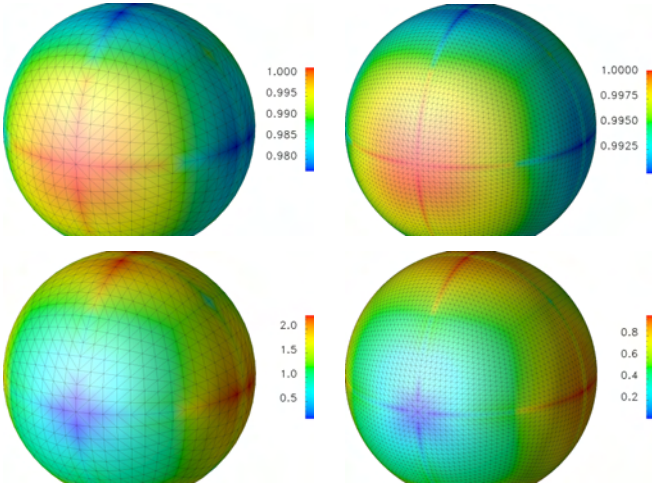| Incoming flow	Unperturbed velocity $\boldsymbol{u}_\infty$	Force $\boldsymbol{F}$	Torque $\boldsymbol{C}$
uniform	$(U_\infty, 0, 0)$	$(6\pi\mu U_\infty \mathcal{R}, 0, 0)$	$\boldsymbol{0}$
shear	$U_\infty(x_2, -x_1, 0)/\mathcal{R}$	$\boldsymbol{0}$	$(0, 0, 8\pi\mu U_\infty \mathcal{R}^2)$
paraboloidal	$U_\infty(x_1^2 + x_2^2, 0, 0)/\mathcal{R}^2$	$(4\pi\mu U_\infty \mathcal{R}, 0, 0)$	$\boldsymbol{0}$

Fig. 2. Colormaps of the nondimensional relative traction $\tau_1^{(\text{GBEM})}/\tau_1^{(\text{analytic})}$ (top) and L_2 norm of the relative percent error (bottom), on the sphere surface using GBEM with a Q_{22} quadrature rule and uniform BEM meshes 5 (left) and 11 (right)

4.1 General data

The numbers of nodes N and of elements E for each BEM mesh z in the sphere and cube cases are shown in Table 1; meshes 1-11 are structured, whereas mesh 12 is an unstructured one only used for the cube case. The modified Taylor "black box" integrator uses a Gauss-Legendre integration rule, with n_{1d} quadrature points along each direction implying a total of n_{1d}^4 points per interaction pair. The effect of varying the number of quadrature points was analyzed, taking into account that typically, more Gauss points are needed for the inner layers. The notation Q_{IJ} is introduced, where the first subindex I notes the number of Gauss-Legendre (GL) points used for the self-integral and for the first layer of neighboring elements, and the second subindex J is the number of Gauss points used for the remaining layers. For instance, a Q_{11} integration rule means one GL point is used for all interaction integrals. Any suitable direct method for linear systems can be used in both cases, although collocation gives a non-symmetric system matrix, whereas Galerkin weighting leads to a positive definite system matrix. In both cases, the system matrices are full and well-conditioned. In particular, Gauss or House-
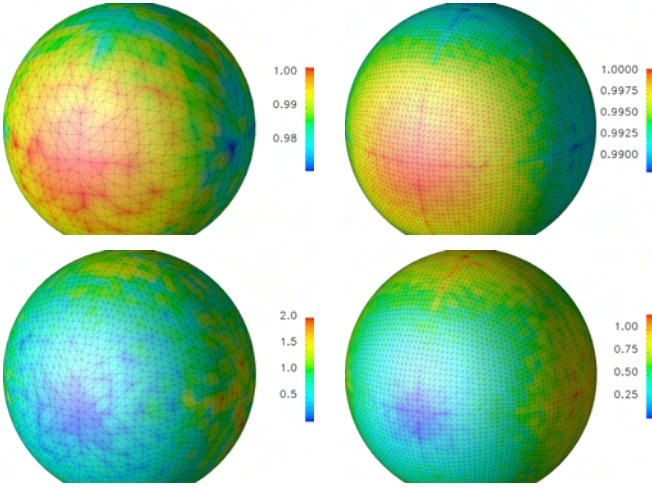
lel flow around the unit cube are also compared with results of a computation based on solving the Navier-Stokes equations using FEM. Next, other geometries with edges and corners, as well as another ones with more intricate shapes are considered. The numerical results obtained with BEM and GBEM are also validated using FEM in some cases.

Fig. 3. Colormaps of the nondimensional traction $\tau_1^{(\text{GBEM})}/\tau_1^{(\text{analytic})}$ (top) and L_2 norm of the relative percent error (bottom), on the sphere surface using GBEM with a Q_{22} quadrature rule and perturbed BEM meshes 8 (left) and 11 (right)

holder solvers can be employed in all cases, and a Cholesky in the second one. In the examples, the absolute value of the relative error $|e_r|$ for the nondimensional body force $\hat{F}$ is computed as $|e_r| = |\hat{F}\text{num}/\hat{F}_{(\text{semi})\text{analytical}} - 1|$. It is plotted as a function of the type of incoming flow, the quadrature rule Q_{IJ} and the number of degrees of freedom M, where $M = 3E$ in collocation schemes and $M = 3N$ in Galerkin schemes. A unit value is used for the Hebeker coupling parameter in all the examples ($\chi_H = 1$).

4.2 Collocation vs. Galerkin BEM. Performance considerations and computational cost

The following considerations can be drawn when comparing performance of collocation and Galerkin implementations: (i) the net forces obtained with Galerkin BEM are more accurate than those obtained with collocation BEM; (ii) Galerkin BEM exhibits monotonic convergence while collocation BEM does not have this property; (iii) the system matrix with Galerkin BEM is symmetric whereas in the case of collocation BEM, it does not have this property; (iv) in Galerkin BEM, the size of the solution vector $\boldsymbol{\psi}$ is $3N$, while it is $3E$ in collocation BEM; since $N \ll E$ for 2D BEM meshes immersed in 3D, then the Galerkin BEM is less expensive than collocation BEM in core-memory

resources, especially when dense matrices are employed, e.g. In general, a Galerkin BEM approach allows to use more refined meshes for a given size of the core memory. All these considerations are supported by the following examples.

4.3 Unit sphere

The sphere test case has analytical solutions for several inflow conditions. In particular, three inflow distributions are considered: uniform, shear, and paraboloidal [33]). Analytical expressions for the unperturbed velocity, force, and torque for each case are summarized in Table 2 [25]. The following values are adopted in the numerical simulations: fluid density $\rho = 1 \text{ kg/m}^3$, kinematic viscosity $\nu = 1 \text{ m}^2/\text{s}$, incoming velocity $U_\infty = 0.001 \text{ m/s}$ along the x_1 direction, and sphere radius $\mathcal{R} = 1 \text{ m}$. The typical length for the computation of nondimensional force, torque and traction is taken equal to the sphere diameter, i.e. $L = 2\mathcal{R} = 2 \text{ m}$.

The exact value of traction on the sphere surface under uniform flow is constant and equal to $\boldsymbol{t} = (3/2)\mu U_\infty/\mathcal{R} \ \boldsymbol{e}_1^0$, where $\boldsymbol{e}_1^0$ is the unit Cartesian vector in the x direction. Figure 2 shows the colormaps of the nondimensional traction $\tau_1 = t_1/(\mu U_\infty L^{-1})$ for the uniform BEM meshes 1, 5 and 11 using GBEM with a Q_{22} quadrature rule.

In order to check the numerical stability of the solution, computations have also been made with perturbed meshes obtained by a random displacement of the nodal positions without leaving the surface of the unit sphere. Figure 3 shows the colormaps of the nondimensional traction τ_1 for the perturbed BEM meshes 6, 8 and 11 using a Q_{22} quadrature rule.

Regarding the sizes of the solution vector with collocation and Galerkin implementations of GBEM, for instance, in the case of mesh 11 in Table 1, there are 20 814 unknowns when using Galerkin BEM ($3N$) and 39 216 unknowns when using collocation BEM ($3E$), i.e. approximately a ratio of 2 to 1. Finally, Fig. 4 shows the elapsed real time [s] (left) and main computer memory (read/write random-access memory (RAM)) in [GB] (right), as a function of the number of elements E, employing a Q_{22} quadrature rule and a direct solver (Gauss method) on 4 of the 6 cores of a Xeon W3690 of 3.47 GHz.
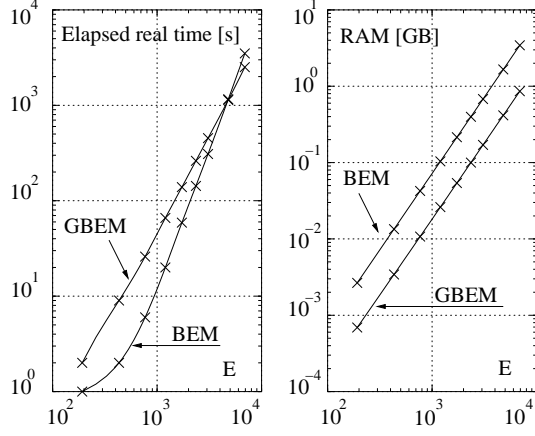
Fig. 4. Computational cost as a function of the number of elements E in the sphere case: elapsed real time [s] (left) and RAM [GB] (right), employing a Q_{22} quadrature rule and a direct solver on 4 of the 6 cores of a Xeon W3690. Collocation (BEM) and Galerkin (GBEM)
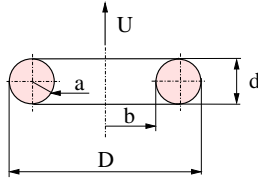

Fig. 5. Sketch for the axisymmetric creeping flow around a torus

4.4 Unit torus

The axisymmetric creeping flow around a torus of unit outer diameter D is considered. In this case, a semi-analytical expression for the drag F_1 exists, given by [34]

$$F_1 = 4\sqrt{2}\pi\mu U_\infty c \sum_{n=0}^{\infty} (nB_n + C_n)$$

$$c = a\sqrt{s_0^2 - 1}$$

(16)

where $s_0 = D/d - 1 = b/a + 1$ is a geometric aspect parameter, $a = d/2$ and $b = D/2 - d$, while D and $2b$ are the major and the minor diameters, see sketch in Fig. 5. The coefficients B_n and C_n are obtained solving a system of linear equations where the coefficients are related to the toroidal harmonics. Equation (16) has been validated by laboratory measurements of the drag at low Reynolds numbers [34].

In the numerical example, a torus with diameters $D = 1$ and $2b = 0.4$ is chosen, which is discretized using a boundary mesh with 2904 nodes

and 5408 elements. The values of the fluid density ρ, kinematic viscosity ν and incoming velocity $\boldsymbol{u}_\infty$ are the same as in the unit sphere.

The nondimensional body force $\hat{F}_1 = F_1/(3\pi U_\infty D)$, with F_1 given by Eq. (16), is $\hat{F}_1 \approx 0.9141$, while the obtained in the numerical simulations, using the Q_{22} quadrature rule, are: $\hat{F}_1 \approx 0.8947$ with collocation, and $\hat{F}_1 \approx 0.8940$ with GBEM (relative errors -2.12 % and -2.20 %, respectively). Further details are given in [35].

4.5 Unit cube

A cube of unit edge length and flat sides, whose center is placed at the origin of coordinates, is analyzed. This example is considered to evaluate the performance of the method to compute flow around a sharp body. This test is selected as a crude simplification of phenomena appearing with MEMS geometries [20, 21]. In the numerical simulations, the following values are adopted: fluid density $\rho = 1.22521$ kg/m^3 and kinematic viscosity $\nu = 1.4528 \times 10^{-5}$ m^2/s (air at sea level and at 15 °C), and edge length $L = 1$ μm $= 10^{-6}$ m.

Five flow patterns are considered, which are summarized in Table 3. Mustakis and Kim [32] calculated asymptotic approximations to the nondimensional surface traction $\tau = O(s^p)$ for these cases in terms of the distance s to the closest vertex, which were verified using low-order, spectral, and B-spline boundary elements.
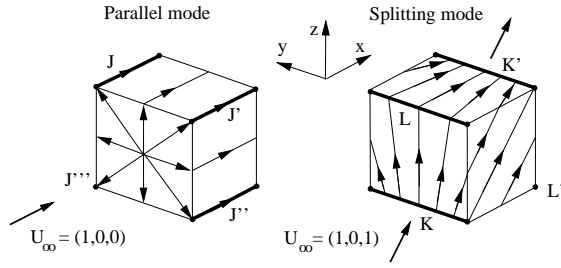
Table 3. The five flow patterns around a rigid cube defined by Mustakis-Kim [32]

Name	flow pattern	$\boldsymbol{u}_\infty$ m/s
FP-1	parallel flow to edges $J - J'''$	$(1, 0, 0)$
FP-2	splitting flow	$(1, 0, 1)$
FP-3	symmetric flow	$(1, 1, 1)$
FP-4	antisymmetric flow I	$(1, 0, -1)$
FP-5	antisymmetric flow II	$(1, -2, 1)$

Fig. 6. Sketch of the quasi 2D steady creeping flow pattern around the rigid cube [32]: (i) parallel flow along edges $J - J'''$; $\boldsymbol{u}_\infty = (1,0,0)$ m/s; (ii) splitting flow $\boldsymbol{u}_\infty = (1,0,1)$ m/s (symmetric on edges K, K' and antisymmetric on edges L, L')

4.5.1 Parallel and splitting flows

The two first flow patterns considered are sketched in Fig. 6:

a) FP-1: flow parallel to edges $J - J'''$, with $\boldsymbol{u}_\infty = (1,0,0)$ m/s, see Fig. 6 (left), giving $p = -0.4555$;

b) FP-2: splitting flow with $\boldsymbol{u}_\infty = (1,0,1)$ m/s, where the flow is splitted at the symmetric edges $K - K'$, giving $p = -0.0915$, and turning around the antisymmetric edges $L - L'$, with $p = -0.3333$, see Fig. 6 (right).

Both flow patterns FP-1 and FP-2 are quasi two–dimensional (2D) in the sense that a 2D wedge flow approximation can be performed close to the edges $J - J'''$, $K - K'$ and $L - L'$.

4.5.2 Symmetric and antisymmetric flow patterns

The third, fourth and fifth flows analyzed are a 3D symmetric pattern and two 3D antisymmetric patterns, as follows:

c) FP-3: symmetric flow with $\boldsymbol{u}_\infty = (1,1,1)$ m/s, giving $p = -0.31877$;

d) FP-4: antisymmetric flow I with $\boldsymbol{u}_\infty = (1,0,-1)$ m/s, giving $p = -0.62463$;

e) FP-5: antisymmetric flow II with $\boldsymbol{u}_\infty = (1,-2,1)$ m/s, giving $p = -0.62463$.

4.5.3 GBEM solution in the unit cube case

A GBEM solution was obtained using the Q_{21} and Q_{22} quadrature rules and mesh 11 (Table 1). It was compared to Mustakis and Kim asymptotic laws, evaluating the nondimensional traction τ along the
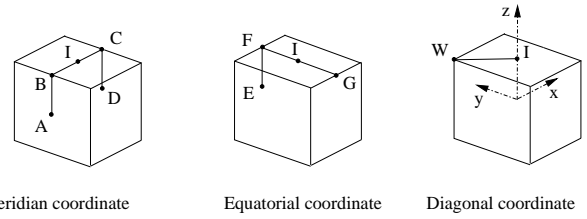

Fig. 7. Meridian, equatorial and diagonal (polygonal) coordinates on the unit cube. The Cartesian coordinate system $O(x,y,z) = O(x_1,x_2,x_3)$ is centered
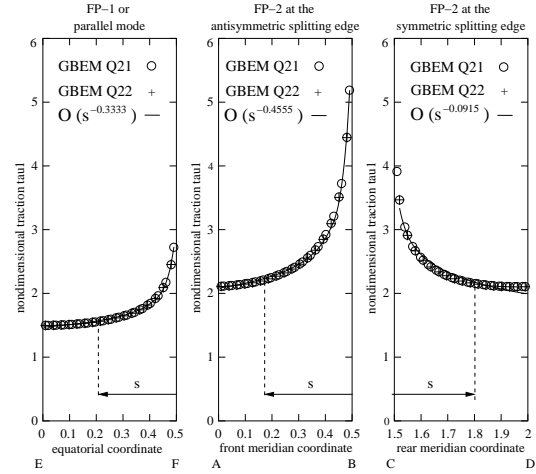

Fig. 8. Quasi 2D steady creeping flow across the middle section of the unit cube: nondimensional traction τ as a function of the coordinate: equatorial EF (left), front meridian AB (center), and rear meridian CD (right). GBEM computation (Q_{21} and Q_{22} rules, mesh 11, Table 1) and semi-analytical laws $O(s^p)$ [32], as a function of the distance s to the edge singularity

polygonal lines: front-meridian AB, rear-meridian CD, equatorial EF and diagonal WI, see Fig. 7.

Figure 8 (left) displays the nondimensional traction along the equatorial line EF for the parallel flow case FP-1. The same figure shows the nondimensional traction along the front-meridian line AB and rear-meridian line CD (center and right plots, respectively) for the splitting flow FP-2. The middle plot is close to the symmetric splitting edges $K - K'$, while the right one is close to the antisymmetric edges $L - L'$.

Figure 9 displays three flow cases: the symmetric flow (FP-3, left), the antisymmetric flow I (FP-4, middle), and the antisymmetric flow II (FP-5, right).

To evaluate the coefficients matrix terms, the Q_{21} quadrature rule gives a time saving of 32 % of the CPU-time, compared to the Q_{22} one.
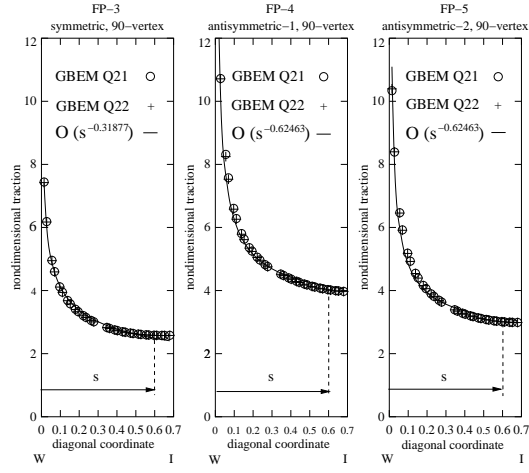
Fig. 9. 3D steady creeping flows of the 90 degree vertex of the unit cube: nondimensional traction τ as a function of the coordinate along the diagonal WI on the top plane. GBEM computation (Q_{21} and Q_{22} rules, mesh 11, Table 1) and semi-analytical laws $O(s^p)$ [32], as a function of the distance s to the vertex singularity
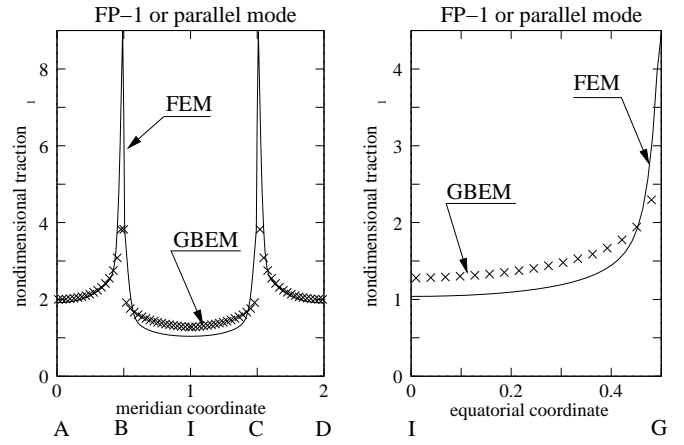

Fig. 10. Cartesian τ_1 component of the nondimensional traction for the parallel flow $\boldsymbol{u} = (U, 0, 0)$ m/s, as a function of the meridional and equatorial coordinates s_m (left) and s_e (right), with FEM (solid line) and GBEM (crosses, using the Q_{22} quadrature rule and mesh 11). See Fig. 7, left and center, for the position of the points $A - I$

4.5.4 FEM solution of the parallel FP-1 case

A FEM computation of the parallel flow $\boldsymbol{u}_\infty = (U_\infty, 0, 0)$ around the unit cube is performed for validation purposes using the open source PETSc-FEM (*URL*: http://www.cimec.org.ar/petscfem) code. This is a parallel multi-physics finite element code [36–38] based on the Message Passing Interface (MPI, http://www.mpi-forum.org) and the Portable Extensible Toolkit for Scientific Computations (PETSc, http://www-fp.mcs.anl.gov/petsc). This code solves the Navier-Stokes equations using linear elements with equal-order interpolations for velocity and pressure fields, stabilized with Streamline Upwind/Petrov-Galerkin (SUPG) [39] and Pressure Stabilizing/Petrov-Galerkin (PSPG) [40]. The steady state is solved at once, i.e. without including the temporal term. Since the FEM computation includes the inertial terms, a very low Reynolds number is chosen in order to compare results with the GBEM ones.

The flow case considered is the parallel flow $\boldsymbol{u}_\infty = (U_\infty, 0, 0)$ m/s, with flow parallel to the edges J-J''' (Fig. 6, left). The Reynolds number is set to $\mathrm{Re} = 0.001$ by choosing kinematic fluid viscosity $\nu = 0.1$ m^2/s, incoming velocity $U_\infty = 10^{-4}$ m/s along the x_1 direction, and cube side length $L = 1$ m. The FEM solution is almost insensitive to the

Reynolds number. The flow is aligned with the x axis and, due to symmetry considerations, only one fourth of the domain ($y, z \geq 0$) is considered. The finite element mesh is built by extrusion of a surface mesh having 50x50 quadrangles on each side of the cube, i.e. it has $50 \times 50 \times 6/4 = 3750$ quadrangles on 1/4 of the cube inside a prismatic domain. The nodal spacing is non-uniform, with a logarithmic refinement towards the edges of the cube, where the results show large friction values. This refinement is such that the linear size h of the quadrangles near the center of the face is in a ratio of 5:1 to the size near the edges. The surface mesh is extruded into 50 layers of hexahedral elements in the radial direction from the cube surface, up to an external cube of length $L_{\mathrm{ext}} = 50$ m. The width of layers in the radial direction is also refined towards the internal cube surface in such a way that the width of the external layer is in a ratio of 40:1 to the layer adjacent to the cube skin. Boundary conditions are as follows: velocity $\boldsymbol{u} = \boldsymbol{u}_\infty$ m/s at inlet ($x = -L_{\mathrm{ext}}/2$), pressure $p = 0$ at outlet ($x = L_{\mathrm{ext}}/2$), slip boundary condition at the lateral walls $y, z = \pm L_{\mathrm{ext}}/2$, and non-slip boundary condition $\boldsymbol{u} = \boldsymbol{0}$ at the cube.

With this setup the computed value for the nondimensional body force is $\hat{F}_1 = F_1/(\mu U_\infty L) \approx 13.760$. The numerical experiment was performed with several values of L_{ext} and mesh refinement in order to assess the sensitivity of this result with

11

respect to those parameters. These series of experiments have shown that this result is particularly sensitive to the size of the computational domain L_{ext}. This is so because the slip boundary conditions are equivalent to a lattice of mirrors of the cube with a spacing of $\Delta y = \Delta z = L_{\text{ext}}$. Then, each cube sees an effective external field given by U_∞ plus the velocity induced by the other cubes in the array. This field decays very slowly (as $O(1/L_{\text{ext}})$) for $L_{\text{ext}} \to \infty$, so that very large domains must be used in order to reduce the error. For instance, the error when using $L_{\text{ext}} = 10$ is estimated in 15%. Computations for a sphere, for which the drag can be computed analytically, show a similar behavior.

The traction map obtained with GBEM is close to the FEM one, whereas the nondimensional body force is approximately 5% lower than the FEM value. This difference is worth commenting on. Both results fall within the interval $(K_{\text{min}}, K_{\text{max}})$ predicted by an analytic computation. In the computation with GBEM, the result is sensitive to the number of quadrature points, whereas for FEM the most influential parameter is the size of the computational domain. In both cases, some residual error may be due to insufficient mesh refinement. This is especially true in the FEM case because the strong variation of friction near the edges degrades the convergence with respect to the mesh refinement. Figure 10 shows the Cartesian τ_1 component of the nondimensional traction of the parallel flow $\boldsymbol{u}_\infty = (U_\infty, 0, 0)$, as a function of the meridian (polygonal) coordinate s_m (left), and as a function of the equatorial one s_e (right), obtained with FEM (solid line) and GBEM (crosses) computation, where the last one was obtained with the Q_{22} quadrature rule and mesh 11.

4.6 Analysis of the solution convergence under mesh refinement

4.6.1 Unit sphere

The absolute value of the relative error $|e_r|$ for the total nondimensional body force $\hat{F}_1$ and body torque $\hat{C}_3$ over the unit sphere is plotted for different quadrature rules Q_{IJ}, and for noisy meshes (Fig. 11). Three incoming flow types are considered: $e_r(\hat{F}_1)$ uniform flow (left), $e_r(\hat{C}_3)$ shear flow (middle) and $e_r(\hat{F}_1)$ paraboloidal flow (right). Note that when GBEM is used, the convergence is
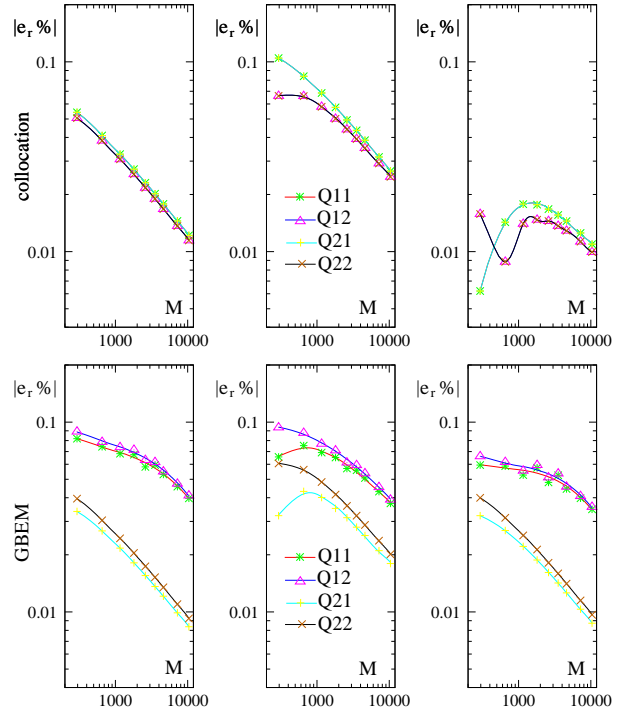

Fig. 11. Absolute value of the relative error $|e_r\%|$ of the nondimensional body force $\hat{F}_1$ and body torque $\hat{C}_3$ as a function of the number of degrees of freedom M and the Q_{IJ} quadrature rule with noisy meshes on the unit sphere: $\hat{F}_1$ uniform flow (left), $\hat{C}_3$ shear flow (center) and $\hat{F}_1$ paraboloidal flow (right). Collocation (top) and GBEM (bottom)

almost monotone whereas collocation BEM does not show a monotonic convergence in all cases (see for instance the incoming paraboloidal flow condition). Note also that, with GBEM convergence is affected when only one Gauss point is used for integrating the inner layers and so the Q_{22} or the Q_{21} Gauss points rules are recommended.

4.6.2 Unit cube

Since there is no analytical solution for the unit cube, bounds and semi-numerical values are taken as a reference. For instance, the drag force is bounded by $F_{\text{min}} < F < F_{\text{max}}$, with $F_{\text{min}} = 3\pi\mu U_\infty L$ and $F_{\text{max}} = \sqrt{3}D_{\text{min}}$, where L is the cube edge length, and $U_\infty = ||\boldsymbol{u}_\infty||_2$. The corresponding nondimensional body force interval is $\hat{F}_{\text{min}} < \hat{F} < \hat{F}_{\text{max}}$, with $\hat{F}_{\text{min}} = 3\pi$ and $\hat{F}_{\text{max}} = 3\sqrt{3}\pi$. The relative errors computed taking as reference the results from the more refined mesh (mesh 11) are plotted in Fig. 12 with a Galerkin BEM (solid line) and with a collocation BEM (dashed line) for: uniform flow (left), shear flow (middle) and paraboloidal
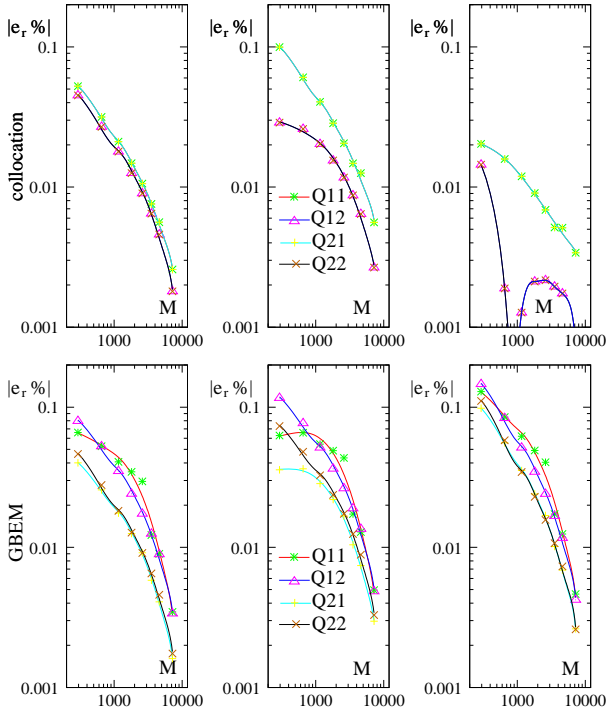
Fig. 12. Absolute value of the relative error $|e_r\%|$ of the nondimensional body force $\hat{F}_1$ and body torque $\hat{C}_3$ as a function of the number of degrees of freedom M and the Q_{IJ} quadrature rule with smooth meshes on the unit cube: $\hat{F}_1$ uniform flow (left), $\hat{C}_3$ shear flow (center) and $\hat{F}_1$ paraboloidal flow (right). Collocation (top) and GBEM (bottom)

flow (right). The nondimensional body force $\hat{F}_1$ and body torque $\hat{C}_3$ over the unit cube obtained with the more refined mesh (mesh 11, Table 1) are: $\hat{F}_1 \approx 13.078$, $\hat{C}_3 \approx 8.716$ and $\hat{F}_1 \approx 3.697$ for uniform, shear and paraboloidal incoming flows, respectively. It is worth noting that the nondimensional body forces obtained in the uniform flow case are close to the geometric mean $\hat{F}_{\mathrm{gm}} = \left(\hat{F}_{\min}\,\hat{F}_{\max}\right)^{1/2}$ given by $\hat{F}_{\mathrm{gm}} = 3\pi\sqrt[4]{3} \approx 12.404$. The nondimensional traction for the 3D steady creeping flows around the cube vertex are plotted in Fig. 9 as a function of the (polygonal) coordinate along the diagonal WI coordinate on the top plane.

In the case of flow parallel to edges J-J''' (parallel flow $\boldsymbol{u}_\infty = (1,0,0)$ m/s, Fig. 8), the nondimensional body force along the x_1-Cartesian direction, computed using mesh 11 and the Q_{22} quadrature rule, is, approximately, $\hat{F}_1 \approx 13.078$. While the proposed scheme is a low-order method, however, the traction on the unit cube shown in Figs. 8-9 compare favorably well compared to those ob-

tained using elements either low order, spectral and B-spline used by Mustakis and Kim [32].

4.7 Other geometries with edges and corners
Other geometries with edges and corners are considered: a concave cube, a hollow cube and a sculpted sphere. The geometries were meshed using NETGEN mesher [41] in all cases. The minimum and maximum nodal coordinates are -1/2 and +1/2, respectively, and the considered flow pattern is the symmetric flow FP-3 (Table 3). The meshes are:

(i) Concave cube (CC): the unit cube is deformed symmetrically in such a way that the six faces of the cube are concave smooth surfaces. For this purpose, the normal displacement $\delta(\xi_i, \xi_j) = \pm 0.2\cos(\pi\xi_i)\cos(\pi\xi_j)$ is applied to the nodes of the mesh, where ξ_i, ξ_j are the local Cartesian coordinates in each plane of the cube and centered at the center of each face (4 706 nodes and 9 408 elements);

(ii) Hollow cube (HC) [41] (4 904 nodes and 9 824 elements): the unit cube is intersected by a sphere and by a complement of a sphere;

(iii) Sculpted sphere (SS) [41] (6 062 nodes and 12 128 elements): the unit sphere is intersected by a smaller one and three cylinders oriented according to the coordinate axes.

These cases have been also solved by FEM, using the PETSc-FEM code by considering a steady state strategy, with the aim of validating the drag forces obtained with collocation and GBEM. With this objective, the fluid domain in each case was proposed large enough to avoid perturbations originated at the channel boundaries. Volume meshes were also generated with NETGEN [41], considering a refinement towards the body surfaces, and such that surface meshes were the same for both BEM and FEM problems. Approximate mesh sizes are the following: the CC was solved with 779 000 tetrahedra and 132 000 nodes; the HC with 805 000 tetrahedra and 155 000 nodes; and the SS with 736 000 tetrahedra and 127 000 nodes. Since the fluid flow is incompressible, velocity is fixed at the inlet section of the channel, and pressure is given at the outlet, while null velocity is applied over all the body surfaces. On the chan-
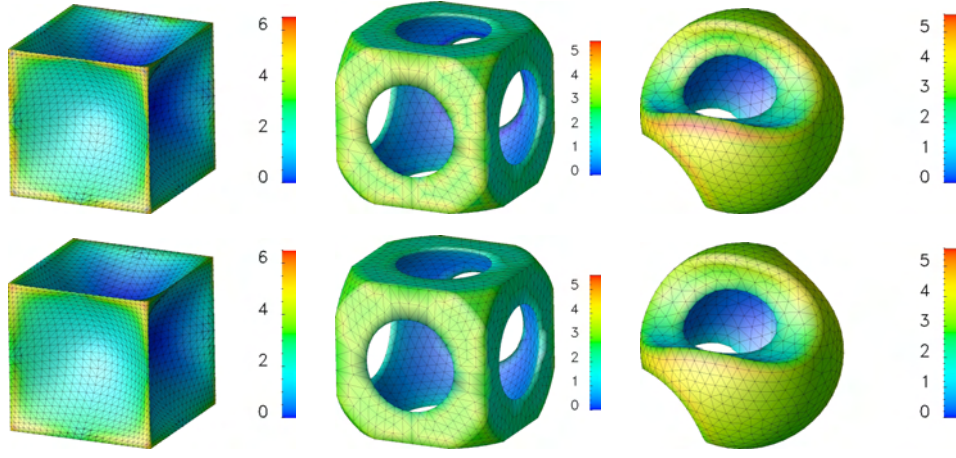
13

Fig. 13. Other geometries with edges and corners: concave cube (left), hollow cube (middle) [41] and sculpted sphere (right) [41]. Colormaps of the τ_1 nondimensional traction for the parallel flow $\boldsymbol{u}_\infty = (1,0,0)$ m/s using the Q_{22} quadrature rule. Collocation (top) and GBEM (bottom)

Table 4. Nondimensional body force $\hat{F}_1$ on the intricate geometries of Figs. 13-14 under uniform flow $(1,0,0)$ m/s. BEM (left), GBEM (middle), and FEM (right)

Geometry	$\hat{F}_1^{\text{BEM}}$	$\hat{F}_1^{\text{GBEM}}$	$\hat{F}_1^{\text{FEM}}$
CC	12.431	12.232	12.106
HC	12.300	12.448	13.136
SS	8.893	9.551	10.052

nel walls, slip conditions were adopted. Kinematic viscosity and reference velocities were chosen to match the same Re number as in BEM simulations.

The GBEM solutions are obtained using the Q_{22} quadrature. The colormaps of the nondimensional traction τ_1 obtained with collocation and GBEM are plotted in Fig. 13, showing the maximum value and their distribution on the body surface. The nondimensional body force $\hat{F}_1$ along the x_1-Cartesian direction obtained with BEM, GBEM and FEM are summarized in Table 4.

4.8 Deliberately intricate 3D geometries

Three deliberately intricate 3D geometries are considered. They are taken from the "180 wrapped tubes" repository [42]. The wrapped tubes case can be considered as a first approximation of twisted fibers or microscopic organisms. The geometries were meshed for BEM/GBEM using the NETGEN mesher [41]. In all cases, the surfaces are not touching each other and enclose a positive finite volume. As in these deliberately intricate 3D geometries are very complicated to perform a volume mesh, the corresponding FEM validations will not be performed. The minimum and maximum nodal coordinates are -1/2 and +1/2, respectively, and the considered flow pattern is the symmetric flow FP-3 (Table 3). Adopting the nomenclature given in both references, the following cases and meshes are chosen:

i) Pentagon knots (case (3, 2/3, -5/5) in [42]): 1 681 nodes and 3 362 elements;

ii) Circle knots (case (2, 3/2) in [42]): 2 578 nodes and 5 156 elements;

iii) Triangle knots (case (1, 3, -6/3) in [42]): 1 364 nodes and 2 728 elements.

The colormaps of the nondimensional traction τ_1 obtained with collocation and GBEM are shown in Fig. 14. The nondimensional traction τ_1 shows an increased intensity near the edges and impact points, and they do not differ significantly from those corresponding to the sphere or cube.

5 Conclusions

A completed indirect velocity boundary integral equation of Fredholm type and second kind has been employed for steady exterior Stokes flow around three–dimensional rigid bodies. It has been numerically solved using collocation and Galerkin
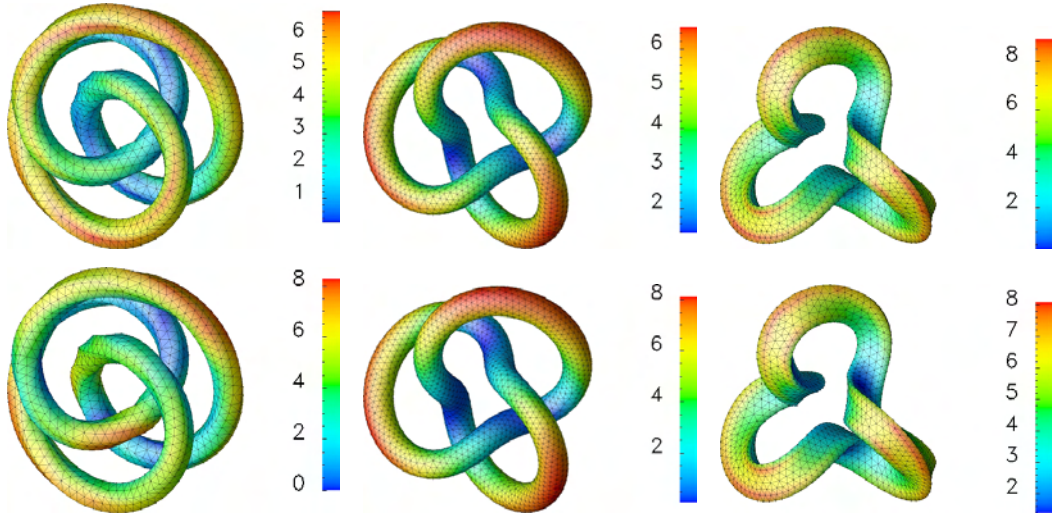
14

Fig. 14. Deliberately intricate 3D geometries using wrapped tubes [42]: pentagon knots (left), circle knots (middle) and triangle knots (right). Collocation (top) and GBEM (bottom)

procedures. The boundary integral equation has been formulated as a combination of double- and single- layer potentials with densities defined over the closed surface. The formulation is an extension of the "completed double-layer boundary integral equation method". In the present strategy, a surface single-layer density has been used, without introducing a surface density of rotlets. Rigid body motions have been filtered assuming that the single-layer density has a linear dependence on the double-layer density, through the free positive parameter of Hebeker χ_H. Numerical experiments showed that the unit value criterion ($\chi_H = 1$) was appropriate to obtain good results. In the Galerkin weighting procedure, the surface integrals that express the pairwise interaction among all elements, have been approximated using an extended Taylor integration scheme, with a full numerical quadrature on the four coordinates in order to handle the weak singularity of the kernels with a general framework. The numerical examples consisted of the steady creeping flow around closed bodies, including bodies with edges and corners, and some deliberately intricate geometries. Issues on the convergence under mesh refinement and numerical stability under small mesh perturbations were analyzed and compared for different formulations.

Different numbers of Gauss–Legendre quadrature points along each direction have been used in the tests. It was noted that with Galerkin BEM, a monotone convergence behavior was attained for all integration rules and incoming flow types. On the other hand, collocation BEM exhibited non–monotone convergence in some cases. A quadrature rule with two Gauss-Legendre points for both the self-integral and first layer of neighboring elements, and one point for the remaining layers has been found to give a reasonable compromise for computation in highly refined meshes, with economy of calculation. The system matrix obtained with a Galerkin technique is fully populated, as in most standard BEM schemes; however, it is symmetric and positive definite which enables a better coupling of BEM and FEM matrices. The traction field was computed using a weakly singular surface integral related to the single-layer surface density. The singular behavior of the surface traction on edges and corners in the unit cube test for some steady creeping flows has been close to the singularity exponents obtained with a semi-analytical computation of Mustakis and Kim. The parallel flow case in the unit cube, concave cube, hollow cube and sculpted sphere has been also validated with a finite element analysis that solve the Navier-Stokes equations. The colormaps of the surface traction and the friction line pattern of the velocity field near edges and corners did not show numerical instabilities nor severe precision loss. Nevertheless, the traction field has been somehow smeared.

References

[1] Beer, G., and Watson, J. O., 1992. *Introduction to Finite and Boundary Element Method for Engineers*. John Wiley and Sons, England.

[2] Sauter, S. A., and Schwab, C., 2011. *Boundary element methods*. Springer.

[3] Stenroos, M., and Haueisen, J., 2008. "Boundary element computations in the forward and inverse problems of electrocardiography: comparison of collocation and Galerkin weightings". *IEEE Trans. on Biomedical Engng.,* **55**(9), September, pp. 2124–2133.

[4] Fata, S. N., 2009. "Explicit expressions for 3D boundary integrals in potential theory". *Int. J. for Num. Meth. in Engng.,* **78**, pp. 32–47.

[5] Scuderi, L., 2008. "On the computation of nearly singular integrals in 3D BEM collocation". *Int. J. for Num. Meth. in Engng.,* **74**, pp. 1733–1770.

[6] D'Elía, J., Storti, M. A., and Idelsohn, S. R., 2000. "A closed form for low order panel methods". *Advances in Engineering Software,* **31**(5), pp. 335–341.

[7] D'Elía, J., Storti, M. A., and Idelsohn, S. R., 2000. "A panel-Fourier method for free surface methods". *J Fluids Eng- Trans ASME,* **122**(2), June, pp. 309–317.

[8] D'Elía, J., Battaglia, L., and Storti, M., 2011. "A semi-analytical computation of the Kelvin kernel for potential flows with a free surface". *Comp. Appl. Math.,* **30**(2), pp. 267–287.

[9] D'Elía, J., Storti, M. A., and Idelsohn, S. R., 2000. "Iterative solution of panel discretizations for potential flows. The modal/multipolar preconditioning". *Int. J. Num. Meth. Fluids,* **32**(1), pp. 1–22.

[10] Alia, A., M., S., and Erchiqui, F., 2006. "Variational boundary element acoustic modelling over mixed quadrilateral–triangular element meshes". *Comm. Numer. Meth. Engng.,* **22**(7), July, pp. 767–780.

[11] Bonnet, M., Maier, G., and Polizzotto, C., 1998. "Symmetric Galerkin boundary element methods". *Appl. Mech. Rev.,* **51**(11), pp. 669–704.

[12] Sutradhar, A., Paulino, G. H., and Gray, L. J., 2008. *Symmetric Galerkin Boundary Element Method*. Springer.

[13] Salvadori, A., 2010. "Analytical integrations in 3D BEM for elliptic problems: evaluation and implementation". *Int. J. for Num. Meth. in Engng.,* **84**(5), pp. 505–542.

[14] Power, H., and Wrobel, L. C., 1995. *Boundary Integral Methods in Fluid Mechanics*. Computational Mechanics Publications, Southampton,UK.

[15] D'Elía, J., Battaglia, L., Storti, M., and Cardona, A., 2009. "Galerkin boundary integral equations applied to three dimensional Stokes flows". In Mecánica Computacional, vol. XXVIII, C. Bauza, P. Lotito, L. Parente, and M. Vénere, eds., pp. 1453–1462.

[16] Ladyzhenskaya, O. A., 1969. *The Mathematical Theory of Viscous Incompressible Flow*, 2 ed. Gordon and Breach Science Publishers.

[17] Dargush, G. F., and Grigoriev, M. M., 2005. "Fast and accurate solutions of steady Stokes flows using multilevel boundary element methods". *J Fluids Eng- Trans ASME,* **127**(4), pp. 640–646.

[18] Lepchev, D., and Weihs, D., 2010. "Low Reynolds number flow in spiral microchannels". *J Fluids Eng- Trans ASME,* **132**(7), p. 071202.

[19] Shipman, T. N., Prasad, A. K., Davidson, S. L., and Cohee, D. R., 2007. "Parti-

cle image velocimetry evaluation of a novel oscillatory-flow flexible chamber mixer". *J Fluids Eng- Trans ASME,* **129**(2), pp. 179–187.

[20] Méndez, C., Paquay, S., Klapka, I., and Raskin, J. P., 2008. "Effect of geometrical nonlinearity on MEMS thermoelastic damping". *Nonlinear Anal. R. World Appl.,* **10**(3), pp. 1579–1588.

[21] Berli, C., and Cardona, A., 2009. "On the calculation of viscous damping of microbeam resonators in air". *J. of Sound and Vibration,* **327**(1-2), pp. 249–253.

[22] Galvis, E., Yarusevych, S., and Culham, J. R., 2012. "Incompressible laminar developing flow in microchannels". *J Fluids Eng- Trans ASME,* **134**(1), pp. 014503–014503–4.

[23] Ingber, M. S., and Mammoli, A. A., 1999. "A comparison of integral formulations for the analysis of low Reynolds number flows". *Eng. Anal. Bound. Elem.,* **23**, pp. 307–315.

[24] Power, H., and Miranda, G., 1987. "Second kind integral equation formulation of Stokes flows past a particle of arbitrary shape". *SIAM J. Appl. Math.,* **47**(4), pp. 689–698.

[25] Kim, S., and Karrila, S. J., 1991. *Microhydrodynamics: Principles and Selected Applications*. Butterwoth-Heinemann.

[26] Ingber, M. S., and Mondy, L. A., 1993. "Direct second kind boundary integral formulation for Stokes flow problems". *Comput. Mech.,* **11**, pp. 11–27.

[27] Fang, Z., Mammoli, A. A., and Ingber, M. S., 2001. "Analyzing irreversibilities in Stokes flows containing suspensed particles using the traction boundary integral equation method". *Eng. Anal. with Boundary Elements,* **25**, pp. 249–257.

[28] Keaveny, E. E., and Shelley, M. J., 2011. "Applying a second-kind boundary integral equation for surface tractions in Stokes flow". *J. Comp. Physics,* **230**, pp. 2141–2159.

[29] Hebeker, F. K., 1986. "Efficient boundary element methods for three-dimensional exterior viscous flow". *Num. Meth. PDE,* **2**(4), Winter, pp. 273–297.

[30] Gonzalez, O., 2009. "On stable, complete, and singularity-free boundary integral formu-

lations of exterior Stokes flow". *SIAM J. Appl. Math.,* **69**, pp. 933–958.

[31] Taylor, D. J., 2003. "Accurate and efficient numerical integration of weakly singulars integrals in Galerkin EFIE solutions". *IEEE Trans. on Antennas and Propag.,* **51**(7), July, pp. 1630–1637.

[32] Mustakis, I., and Kim, S., 1998. "Microhydrodynamics of sharp corners and edges: traction singularities". *AIChE Journal,* **44**(7), pp. 1469–1483.

[33] Pozrikidis, C., 1997. *Boundary Integral and Singularity Methods for Linearized Viscous Flow*. Cambridge University Press.

[34] Amarakoon, A. M. D., Hussey, R. G., Good, B. J., and Grimsal, E. G., 1982. "Drag measurements for axisymmetric motion of a torus at low Reynolds number". *Phys. Fluids,* **25**(9), pp. 1495–1501.

[35] Sarraf, S., López, E., Ríos Rodríguez, G., and D'Elía, J., 2013. "Validation of a Galerkin technique on a boundary integral equation for creeping flow around a torus". *Comp. Appl. Math.*, pp. 1–18.

[36] Storti, M. A., Nigro, N. M., Paz, R. R., and Dalcin, L. D., 2008. "Dynamic boundary conditions in computational fluid dynamics". *Comp. Meth. in Appl. Mech. and Engr.,* **197**(13-16), pp. 1219–1232.

[37] Battaglia, L., D'Elía, J., Storti, M. A., and Nigro, N. M., 2006. "Numerical simulation of transient free surface flows". *J App Mech-Trans ASME,* **73**(6), November, pp. 1017–1025.

[38] Storti, M. A., and D'Elía, J., 2004. "Added mass of an oscillating hemisphere at very-low and very-high frequencies". *J Fluids Eng-Trans ASME,* **126**(6), November, pp. 1048–1053.

[39] Brooks, A. N., and Hughes, T. J. R., 1982. "Streamline upwind/Petrov–Galerkin formulations for convection dominated flows with particular emphasis on the incompressible Navier-Stokes equations". *Comp. Meth. App. Mech. Engng.,* **32**, pp. 199–259.

[40] Tezduyar, T. E., Mittal, S., Ray, S., and Shih, R., 1992. "Incompressible flow computations with stabilized bilinear and linear

equal order interpolation velocity-pressure elements". *Comp. Meth. App. Mech. Engng.,* **95**, pp. 221–242.

[41] Schöberl, J., 2012. NETGEN 4.3 mesher. Tech. rep., University of Linz, Austria, http://sourceforge.net/projects/netgen-mesher/.

[42] Edelsbrunner, H., 2012. 180 wrapped tubes. Tech. rep., Department of Computer Science, Duke University, Durham, http://www.cs.duke.edu/-edels/Tubes/.

[43] D'Elía, J., Battaglia, L., Cardona, A., and Storti, M., 2011. "Full numerical quadrature of weakly singular double surface integrals in Galerkin boundary element methods". *Int. J. for Num. Meth. in Biomedical Engng.,* **27**(2), pp. 314–334.

[44] Polimeridis, A. G., and Mosig, J. R., 2010. "Complete semi-analytical treatment of weakly singular integrals on planar triangles via the direct evaluation method". *Int. J. for Num. Meth. in Engng.,* **83**(12), pp. 1625–1650.

Appendix A: The Power-Miranda formulation
Power and Miranda [24] identified the supplementary flow $\mathcal{V}$ with the one produced by a point force and a rotlet, setting [33]

$$v_i(\boldsymbol{x}) = w_i^{\mathrm{DL}}(\boldsymbol{x}; \boldsymbol{\psi}) + q_{ik}(\boldsymbol{x})\alpha_k + r_{ik}(\boldsymbol{x})\beta_k \qquad (17)$$

for all $\boldsymbol{x} \in \Omega^e$, where $w_i^{\mathrm{DL}}(\boldsymbol{x}; \boldsymbol{\psi})$ is the perturbation velocity due to the potential produced by the DL density $\boldsymbol{\psi}$, whereas

$$q_{ik}(\boldsymbol{x}) = -\frac{1}{8\pi\mu}\left[\frac{\delta_{ik}}{R} + \frac{x_i x_k}{R^3}\right] \qquad (18)$$

is the Stokeslet [33], and

$$r_{ik}(\boldsymbol{x}) = -\frac{1}{8\pi\mu}\frac{\varepsilon_{ipq}\delta_{pk}x_q}{R^3} \qquad (19)$$

is the rotlet [33]. In the expressions above δ_{ik} is the Kronecker delta and ε_{ijk} is the Levi-Civita (or third-order permutation) symbol. Thus, this formulation adds to the DL potential, a Stokeslet of strength α_k and a rotlet of strength β_k, both located at the origin. The Stokeslet exerts a total force equal to its strength and a zero total torque on any closed surface enclosing it, whereas the rotlet exerts a total torque equal to its strength and zero total force on any closed surface enclosing it. Meanwhile, the potential with a well-defined DL surface density $\boldsymbol{\psi}$ yields zero total force and torque on the closed surface A. Therefore, the total force and torque resulting from the flow field defined by Eq. (17) are equal to the strengths $\boldsymbol{\alpha}$ and $\boldsymbol{\beta}$, respectively ([14] (Sec. 6.2, p. 196)). If the DL density $\boldsymbol{\psi}$ is sufficiently smooth, it is known that the related velocity $w_i^{\mathrm{DL}}(\boldsymbol{x}; \boldsymbol{\psi})$ satisfies the jump property across a closed surface A (e.g. see [16], Sec. 3.2, Eq. 22, p. 57)),

$$\boldsymbol{w}^{\mathrm{DL}}(\boldsymbol{x}; \boldsymbol{\psi})_{(i)} - \boldsymbol{w}^{\mathrm{DL}}(\boldsymbol{x}; \boldsymbol{\psi})_{(e)} = \boldsymbol{\psi}(\boldsymbol{x}) \qquad (20)$$

where $\boldsymbol{x} \in A$, while subscripts (i) and (e) denote the limit values of $\boldsymbol{w}^{\mathrm{DL}}(\boldsymbol{x}; \boldsymbol{\psi})$ from inside or outside of the surface A, respectively. They are given by

$$w_i^{\mathrm{DL}}(\boldsymbol{x}; \boldsymbol{\psi})_{(i)} = +\frac{1}{2}\psi_i(\boldsymbol{x}) + w_i^{\mathrm{DL}}(\boldsymbol{x}; \boldsymbol{\psi})$$
$$w_i^{\mathrm{DL}}(\boldsymbol{x}; \boldsymbol{\psi})_{(e)} = -\frac{1}{2}\psi_i(\boldsymbol{x}) + w_i^{\mathrm{DL}}(\boldsymbol{x}; \boldsymbol{\psi}) \qquad (21)$$

whereas $w_i^{\mathrm{DL}}(\boldsymbol{x}; \boldsymbol{\psi})$ denotes the direct value of $w_i^{\mathrm{DL}}(\boldsymbol{x}; \boldsymbol{\psi})$ on the surface A, and it is given by Eq. (4). It is known that on smooth surfaces [25],

$$\int_A \tilde{K}_{ij}(\boldsymbol{x}, \boldsymbol{y}) \, \mathrm{d}A_{\boldsymbol{y}} = \frac{1}{2}\delta_{ij} \qquad (22)$$

where $\tilde{K}_{ij}$ is given by Eq. (4). On the other hand, if the SL density $\boldsymbol{\phi}$ is smooth enough, bounded and integrable, then the related velocity $\boldsymbol{w}^{\mathrm{SL}}(\boldsymbol{x}; \boldsymbol{\phi})$ is continuous in the whole space $\mathbb{R}^3$, i.e.

$$\boldsymbol{w}^{\mathrm{SL}}(\boldsymbol{x}; \boldsymbol{\phi})_{(i)} = \boldsymbol{w}^{\mathrm{SL}}(\boldsymbol{x}; \boldsymbol{\phi})_{(e)} = \boldsymbol{w}^{\mathrm{SL}}(\boldsymbol{x}; \boldsymbol{\phi}) \qquad (23)$$

Appendix B: The Hebeker formulation

In the Hebeker formulation, the perturbed velocity $v_i(\boldsymbol{x})$ is thought of as the sum of the DL and SL velocities, i.e.

$$v_i(\boldsymbol{x}) = w_i^{\mathrm{DL}}(\boldsymbol{x};\boldsymbol{\psi}) + w_i^{\mathrm{SL}}(\boldsymbol{x};\boldsymbol{\phi}) \quad \text{for all } \boldsymbol{x} \in \Omega^e \tag{24}$$

Since the SL density $\boldsymbol{\phi}$ is equivalent to a continuous distribution of point forces on the surface A, this potential is able to exert a net torque on the body and, then, it is not necessary to introduce any rotlet. Next, replacing Eq. (8) into Eq. (5) results

$$w_i^{\mathrm{SL}}(\boldsymbol{x};\boldsymbol{\psi}) = \chi_H \int_A \hat{S}_{ij}(\boldsymbol{x},\boldsymbol{y})\psi_j(\boldsymbol{y})\,\mathrm{d}A_{\boldsymbol{y}} \tag{25}$$

with $\hat{S}_{ij}$ given by Eq. (5). Then, Eq. (24) is rewritten as

$$v_i(\boldsymbol{x}) = w_i^{\mathrm{DL}}(\boldsymbol{x};\boldsymbol{\psi}) + w_i^{\mathrm{SL}}(\boldsymbol{x};\boldsymbol{\psi}) \quad \text{for all } \boldsymbol{x} \in \Omega^e. \tag{26}$$

Replacing Eq. (26) into the no-slip boundary condition on the body surface A, given by Eq. (2)

$$w_i^{\mathrm{DL}}(\boldsymbol{x};\boldsymbol{\psi})_{(e)} + w_i^{\mathrm{SL}}(\boldsymbol{x};\boldsymbol{\psi})_{(e)} + u_i(\boldsymbol{x}) = 0 \tag{27}$$

for all $\boldsymbol{x} \in A$. Replacing $w_i^{\mathrm{DL}}(\boldsymbol{x};\boldsymbol{\psi})_{(e)}$ and $w_i^{\mathrm{SL}}(\boldsymbol{x};\boldsymbol{\psi})_{(e)}$ by the exterior limit case of Eqs. (21) and (23), respectively,

$$-\frac{1}{2}\psi_i(\boldsymbol{x}) + w_i^{\mathrm{DL}}(\boldsymbol{x};\boldsymbol{\psi}) + w_i^{\mathrm{SL}}(\boldsymbol{x};\boldsymbol{\psi}) = -u_i(\boldsymbol{x}) \tag{28}$$

for all $\boldsymbol{x} \in A$. By using the identity $\psi_i(\boldsymbol{x}) = \delta_{ij}\psi_j(\boldsymbol{x})$, and replacing $w_i^{\mathrm{DL}}(\boldsymbol{x};\boldsymbol{\psi})$ and $w_i^{\mathrm{SL}}(\boldsymbol{x};\boldsymbol{\psi})$ by Eqs. (4) and (25), respectively, and dropping the arguments in the kernels $\tilde{K}_{ij}(\boldsymbol{x},\boldsymbol{y})$ and $\tilde{S}_{ij}(\boldsymbol{x},\boldsymbol{y})$ for simplicity in the notation, results

$$-\frac{1}{2}\delta_{ij}\psi_j(\boldsymbol{x}) + \int_A \tilde{K}_{ij}\psi_j(\boldsymbol{y})\,\mathrm{d}A_{\boldsymbol{y}}$$
$$+\chi_H \int_A \tilde{S}_{ij}\psi_j(\boldsymbol{y})\,\mathrm{d}A_{\boldsymbol{y}} = -u_i(\boldsymbol{x}) \tag{29}$$

for all $\boldsymbol{x} \in A$. Using Eq. (22) in the first term on the left hand side of Eq. (29), introducing $\psi_j(\boldsymbol{x})$ into the integral sign, and rearranging, Eqs. (9-10) are obtained.

Appendix C: Numerical formulations
Collocation using constant elements

Assuming that the DL density layer $\boldsymbol{\psi}$ on the surface of each element is constant, it can be extracted out of the surface integrals in Eq. (9) and using a standard collocation technique, it results in the system of equations

$$\sum_{q=1}^{E} \left[\int_{A^{(q)}} \tilde{\boldsymbol{K}}^{(p,q)}\,\mathrm{d}A_{\boldsymbol{y}}\boldsymbol{\psi}^{(p)} \right. $$
$$\left. - \int_{A^{(q)}} \tilde{\boldsymbol{H}}^{(p,q)}\,\mathrm{d}A_{\boldsymbol{y}}\boldsymbol{\psi}^{(q)} \right] = \boldsymbol{u}^{(p)} \tag{30}$$

where the elemental matrices $\tilde{\boldsymbol{H}}^{(p,q)} = \tilde{\boldsymbol{H}}(\boldsymbol{x}^{(p)},\boldsymbol{x}^{(q)})$ and $\tilde{\boldsymbol{K}}^{(p,q)} = \tilde{\boldsymbol{K}}(\boldsymbol{x}^{(p)},\boldsymbol{x}^{(q)})$, as well as the vectors $\boldsymbol{\psi}^{(p)} = \boldsymbol{\psi}(\boldsymbol{x}^{(p)})$, $\boldsymbol{\psi}^{(q)} = \boldsymbol{\psi}(\boldsymbol{x}^{(q)})$ and $\boldsymbol{u}^{(p)} = \boldsymbol{u}(\boldsymbol{x}^{(p)})$ are evaluated at the element centroids $\boldsymbol{x}^{(p)}$ and $\boldsymbol{x}^{(q)}$, respectively, for $p,q = 1,2,...,E$. By reordering

$$(\boldsymbol{W} - \chi_H \boldsymbol{S})\boldsymbol{\psi} = \boldsymbol{u} \tag{31}$$

where

$$\boldsymbol{\psi} = \left[\boldsymbol{\psi}^{(1)}\ \boldsymbol{\psi}^{(2)}\ ...\ \boldsymbol{\psi}^{(E)}\right]^T \in \mathbb{R}^{3E \times 1}$$
$$\boldsymbol{u} = \left[\boldsymbol{u}^{(1)}\ \boldsymbol{u}^{(2)}\ ...\ \boldsymbol{u}^{(E)}\right]^T \in \mathbb{R}^{3E \times 1} \tag{32}$$

are global vectors. The global matrices $\boldsymbol{W}$ and $\boldsymbol{S}$ are given by the sums

$$\boldsymbol{W} = \sum_{q=1}^{E} \boldsymbol{W}^{(p,q)}$$
$$\boldsymbol{S} = \sum_{q=1}^{E} \boldsymbol{S}^{(p,q)} \tag{33}$$

respectively, with $p = 1,2,...,E$, where

$$\boldsymbol{W}^{(p,q)} = \begin{cases} \displaystyle\sum_{q=1,q\neq p}^{E} \boldsymbol{K}^{(p,q)} & \text{when } q = p \\[2mm] -\boldsymbol{K}^{(p,q)} & \text{otherwise} \end{cases} \tag{34}$$

19

and the elemental matrices are defined as

$$K^{(p,q)} = \int_{A^{(q)}} \tilde{K}^{(p,q)} \, dA_y$$
$$S^{(p,q)} = \int_{A^{(q)}} \tilde{S}^{(p,q)} \, dA_y \tag{35}$$

It is known that the system of equations (31) is regular and well conditioned [2, 14].

Galerkin weighting using linear elements

Linear approximations $\hat{\boldsymbol{\psi}}^{(p,q)}$ and $\hat{\boldsymbol{u}}^{(q)}$ for the densities $\boldsymbol{\psi}^{(p,q)}(\boldsymbol{x}) \in \mathbb{R}^{3\times 1}$ and velocity $\boldsymbol{u}^{(q)}(\boldsymbol{x}) \in \mathbb{R}^{3\times 1}$ fields are assumed, respectively, on the surface of the p and q simplex triangles, that is,

$$\boldsymbol{\psi}^{(p)}(\boldsymbol{x}) \approx \hat{\boldsymbol{\psi}}^{(p)} = \boldsymbol{N}^{(p)}(\boldsymbol{x})\boldsymbol{\psi}^{(p)}$$
$$\boldsymbol{\psi}^{(q)}(\boldsymbol{x}) \approx \hat{\boldsymbol{\psi}}^{(q)} = \boldsymbol{N}^{(q)}(\boldsymbol{x})\boldsymbol{\psi}^{(q)} \tag{36}$$
$$\boldsymbol{u}^{(q)}(\boldsymbol{x}) \approx \hat{\boldsymbol{u}}^{(q)} = \boldsymbol{N}^{(q)}(\boldsymbol{x})\boldsymbol{u}^{(q)}$$

where the element shape functions $\boldsymbol{N}^{(p,q)}(\boldsymbol{x}) \in \mathbb{R}^{3\times 9}$ are given by

$$\boldsymbol{N}^{(p)}(\boldsymbol{x}) = \left[\boldsymbol{N}_i^{(p)}(\boldsymbol{x}) \, \boldsymbol{N}_j^{(p)}(\boldsymbol{x}) \, \boldsymbol{N}_k^{(p)}(\boldsymbol{x})\right]$$
$$\boldsymbol{N}^{(q)}(\boldsymbol{x}) = \left[\boldsymbol{N}_r^{(q)}(\boldsymbol{x}) \, \boldsymbol{N}_s^{(q)}(\boldsymbol{x}) \, \boldsymbol{N}_t^{(q)}(\boldsymbol{x})\right] \tag{37}$$

respectively, which are the restrictions of the nodal shape functions $\boldsymbol{N}_i(\boldsymbol{x})$, $\boldsymbol{N}_j(\boldsymbol{x})$ and $\boldsymbol{N}_k(\boldsymbol{x})$ on the p element, and $\boldsymbol{N}_r(\boldsymbol{x})$, $\boldsymbol{N}_s(\boldsymbol{x})$ and $\boldsymbol{N}_t(\boldsymbol{x})$ on the q element, respectively, while the global node numbers of the triangles p and q are the counterclockwise sequences (i, j, k) and (r, s, t), respectively, see Fig. 15. The vectors $\boldsymbol{\psi}^{(p)}$ and $\boldsymbol{\psi}^{(q)}$ are given by

$$\boldsymbol{\psi}^{(p)} = \begin{bmatrix} \boldsymbol{\psi}_i \\ \boldsymbol{\psi}_j \\ \boldsymbol{\psi}_k \end{bmatrix} \in \mathbb{R}^{9\times 1} \quad \text{and} \quad \boldsymbol{\psi}^{(q)} = \begin{bmatrix} \boldsymbol{\psi}_r \\ \boldsymbol{\psi}_s \\ \boldsymbol{\psi}_t \end{bmatrix} \in \mathbb{R}^{9\times 1} \tag{38}$$

with

$$\boldsymbol{\psi}_h = \begin{bmatrix} \psi_{3h-2} \\ \psi_{3h-1} \\ \psi_{3h} \end{bmatrix} \in \mathbb{R}^{3\times 1} \tag{39}$$

for nodes $1 \leq h \leq N$, where N is the number of nodes on the boundary mesh, while the element source vector is

$$\boldsymbol{u}^{(p)} = \begin{bmatrix} \boldsymbol{u}_i \\ \boldsymbol{u}_j \\ \boldsymbol{u}_k \end{bmatrix} \in \mathbb{R}^{9\times 1} \quad \text{with} \quad \boldsymbol{u}_h = \begin{bmatrix} U_{3h-2} \\ U_{3h-1} \\ U_{3h} \end{bmatrix} \in \mathbb{R}^{3\times 1} \tag{40}$$

The standard Galerkin weighting technique employs the shape functions $\boldsymbol{N}_h(\boldsymbol{x})$ to enforce Eq. (11) through the orthogonality conditions

$$\int_A \boldsymbol{N}_h^T(\boldsymbol{x})\hat{\boldsymbol{g}}(\boldsymbol{x}) \, dA_{\boldsymbol{x}} = \int_A \boldsymbol{N}_h^T(\boldsymbol{x})\hat{\boldsymbol{u}}(\boldsymbol{x}) \, dA_{\boldsymbol{x}} \tag{41}$$

for nodes $h = 1, 2, ..., N$, where N is the number of nodes on the boundary mesh, and the supra-index T denotes transposition. The nodal shape functions on Eq. (41) are arranged as

$$\boldsymbol{N}^T(\boldsymbol{x}) = \begin{bmatrix} \boldsymbol{N}_1^T(\boldsymbol{x}) \\ ... \\ \boldsymbol{N}_h^T(\boldsymbol{x}) \\ ... \\ \boldsymbol{N}_N^T(\boldsymbol{x}) \end{bmatrix} \in \mathbb{R}^{3N\times 3} \tag{42}$$

with

$$\boldsymbol{N}_h^T(\boldsymbol{x}) = \begin{bmatrix} N_h(\boldsymbol{x}) & 0 & 0 \\ 0 & N_h(\boldsymbol{x}) & 0 \\ 0 & 0 & N_h(\boldsymbol{x}) \end{bmatrix} \tag{43}$$

and

$$N_h(\boldsymbol{x}) = \sum_{e\in\text{patch(h)}} N_h^{(e)}(\boldsymbol{x}) \tag{44}$$

where patch(h) is the patch of adjacent elements around the h node. In what follows, the order $\int dz \int dy \int dx \, f(x,y,z)$ is used, where the integrations are performed from right to left, instead of $\int\int\int f(x,y,z) \, dx \, dy \, dz$. The functions $\hat{\boldsymbol{g}}(\boldsymbol{x}), \hat{\boldsymbol{u}}(\boldsymbol{x}) \in \mathbb{R}^{3\times 1}$ in Eq. (41) are given by

$$\boldsymbol{g}(\boldsymbol{x}) \approx \hat{\boldsymbol{g}}(\boldsymbol{x}) = \sum_{p=1}^{E} \hat{\boldsymbol{g}}^{(p)}(\boldsymbol{x}) \tag{45}$$

and

$$\boldsymbol{u}(\boldsymbol{x}) \approx \hat{\boldsymbol{u}}(\boldsymbol{x}) = \sum_{p=1}^{E} \hat{\boldsymbol{u}}^{(p)}(\boldsymbol{x}) = \sum_{p=1}^{E} \boldsymbol{N}^{(p)}(\boldsymbol{x}) \boldsymbol{u}^{(p)} \quad (46)$$

respectively, where

$$\hat{\boldsymbol{g}}^{(p)}(\boldsymbol{x}) = \sum_{q=1}^{E} \hat{\boldsymbol{g}}^{(p,q)}(\boldsymbol{x}) \qquad \text{with}$$

$$\hat{\boldsymbol{g}}^{(p,q)}(\boldsymbol{x}) = \int_{A^{(q)}} \mathrm{d}A_{\boldsymbol{y}} \quad (47)$$
$$\times \left[\boldsymbol{K}(\boldsymbol{x},\boldsymbol{y}) \hat{\boldsymbol{\psi}}^{(p)}(\boldsymbol{x}) - \boldsymbol{H}(\boldsymbol{x},\boldsymbol{y}) \hat{\boldsymbol{\psi}}^{(q)}(\boldsymbol{y}) \right]$$

and $\boldsymbol{u}^{(p)}$ is given by

$$\boldsymbol{u}^{(p)} = \begin{bmatrix} \boldsymbol{u}_i \\ \boldsymbol{u}_j \\ \boldsymbol{u}_k \end{bmatrix} \in \mathbb{R}^{9 \times 1} \quad \text{with} \quad \boldsymbol{u}_i = \begin{bmatrix} U_{3i-2} \\ U_{3i-1} \\ U_{3i} \end{bmatrix} \in \mathbb{R}^{3 \times 1}$$
$$(48)$$

Taking into account the compact support of the nodal shape functions $\boldsymbol{N}_h(\boldsymbol{x})$, replacing Eqs. (45-47) into Eq. (41) results

$$\sum_{p=1}^{E} \hat{\boldsymbol{g}}^{(p)} = \sum_{p=1}^{E} \hat{\boldsymbol{b}}^{(p)} \quad (49)$$

The left hand side of Eq. (49) leads to the system matrix of the Galerkin approximation, i.e.

$$\hat{\boldsymbol{g}}^{(p)} = \int_{A^{(p)}} \mathrm{d}A_{\boldsymbol{x}} \left\{ \boldsymbol{N}^{(p)T}(\boldsymbol{x}) \sum_{q=1}^{E} \hat{\boldsymbol{g}}^{(p,q)}(\boldsymbol{x}) \right\}$$
$$= \int_{A^{(p)}} \mathrm{d}A_{\boldsymbol{x}} \left\{ \boldsymbol{N}^{(p)T}(\boldsymbol{x}) \sum_{q=1}^{E} \int_{A^{(q)}} \mathrm{d}A_{\boldsymbol{y}} \right.$$
$$\left. \times \left[\boldsymbol{K}(\boldsymbol{x},\boldsymbol{y}) \hat{\boldsymbol{\psi}}^{(p)}(\boldsymbol{x}) - \boldsymbol{H}(\boldsymbol{x},\boldsymbol{y}) \hat{\boldsymbol{\psi}}^{(q)}(\boldsymbol{y}) \right] \right\}$$
$$= \hat{\boldsymbol{g}}_1^{(p)} + \hat{\boldsymbol{g}}_2^{(p)}$$
$$(50)$$

where

$$\hat{\boldsymbol{g}}_1^{(p)} = \sum_{q=1}^{E} \int_{A^{(p)}} \mathrm{d}A_{\boldsymbol{x}} \int_{A^{(q)}} \mathrm{d}A_{\boldsymbol{y}}$$
$$\times \left[\boldsymbol{N}^{(p)T}(\boldsymbol{x}) \, \boldsymbol{K}(\boldsymbol{x},\boldsymbol{y}) \, \boldsymbol{N}^{(p)}(\boldsymbol{x}) \right] \boldsymbol{\psi}^{(p)} \quad (51)$$
$$= \sum_{q=1}^{E} \boldsymbol{I}^{(p,q)} \boldsymbol{\psi}^{(p)}$$

and

$$\hat{\boldsymbol{g}}_2^{(p)} = \sum_{q=1}^{E} \int_{A^{(p)}} \mathrm{d}A_{\boldsymbol{x}} \int_{A^{(q)}} \mathrm{d}A_{\boldsymbol{y}}$$
$$\times \left[\boldsymbol{N}^{(p)T}(\boldsymbol{x}) \, \boldsymbol{H}(\boldsymbol{x},\boldsymbol{y}) \, \boldsymbol{N}^{(q)}(\boldsymbol{y}) \right] \boldsymbol{\psi}^{(q)} \quad (52)$$
$$= \sum_{q=1}^{E} \boldsymbol{J}^{(p,q)} \boldsymbol{\psi}^{(q)}$$

while the $\boldsymbol{I}^{(p,q)}$ and $\boldsymbol{J}^{(p,q)}$ matrices are given by

$$\boldsymbol{I}^{(p,q)} = \int_{A^{(p)}} \mathrm{d}A_{\boldsymbol{x}} \int_{A^{(q)}} \mathrm{d}A_{\boldsymbol{y}}$$
$$\times \left[\boldsymbol{N}^{(p)T}(\boldsymbol{x}) \, \boldsymbol{K}(\boldsymbol{x},\boldsymbol{y}) \, \boldsymbol{N}^{(p)}(\boldsymbol{x}) \right] \quad (53)$$

and

$$\boldsymbol{J}^{(p,q)} = \int_{A^{(p)}} \mathrm{d}A_{\boldsymbol{x}} \int_{A^{(q)}} \mathrm{d}A_{\boldsymbol{y}}$$
$$\times \left[\boldsymbol{N}^{(p)T}(\boldsymbol{x}) \, \boldsymbol{H}(\boldsymbol{x},\boldsymbol{y}) \, \boldsymbol{N}^{(q)}(\boldsymbol{y}) \right] \quad (54)$$

respectively. Finally, the second term of Eq. (49) gives the right hand side of the Galerkin system and it is given by

$$\hat{\boldsymbol{b}}^{(p)} = \int_{A^{(p)}} \mathrm{d}A_{\boldsymbol{x}} \, \boldsymbol{N}^{(p)T}(\boldsymbol{x}) \hat{\boldsymbol{u}}^{(p)}(\boldsymbol{x})$$
$$= \int_{A^{(p)}} \mathrm{d}A_{\boldsymbol{x}} \left[\boldsymbol{N}^{(p)T}(\boldsymbol{x}) \, \boldsymbol{N}^{(p)}(\boldsymbol{x}) \right] \boldsymbol{u}^{(p)}$$
$$= \boldsymbol{M}^{(p)} \boldsymbol{u}^{(p)}$$
$$(55)$$

where the $\boldsymbol{M}^{(p)}$ matrix is given by

$$\boldsymbol{M}^{(p)} = \int_{A^{(p)}} \mathrm{d}A_{\boldsymbol{x}} \left[\boldsymbol{N}^{(p)T}(\boldsymbol{x}) \boldsymbol{N}^{(p)}(\boldsymbol{x}) \right] \quad (56)$$

Then, Eq. (41) results in the system of equations

$$\sum_{p=1}^{E} \sum_{q=1}^{E} \left[\boldsymbol{I}^{(p,q)} \boldsymbol{\psi}^{(p)} - \boldsymbol{J}^{(p,q)} \boldsymbol{\psi}^{(q)} \right] = \sum_{p=1}^{E} \boldsymbol{M}^{(p)} \boldsymbol{u}^{(p)}$$
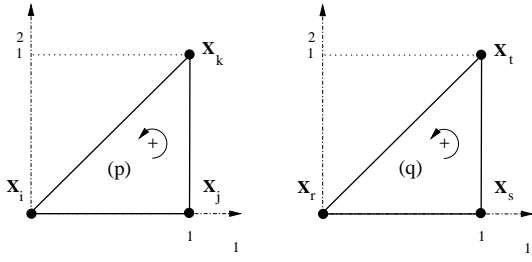$$(57)$$

Fig. 15. Master triangles p and q for the simplex coordinates

Double-surface integrals over flat triangles with a weak singularity

The interaction integrals $\boldsymbol{I}^{(p,q)}$ and $\boldsymbol{J}^{(p,q)}$ given by Eqs. (53) and (54), respectively, involve double-surface integrals of the form

$$\boldsymbol{Z} = \int_{A^{(p)}} \int_{A^{(q)}} \boldsymbol{L}(\boldsymbol{x},\boldsymbol{y}) \, \mathrm{d}A_{\boldsymbol{y}} \, \mathrm{d}A_{\boldsymbol{x}} \qquad (58)$$

performed over elements p and q. This is a quadruple integral, whose integrand can be written as a multiplicative kernel $\boldsymbol{L} = \boldsymbol{R}\boldsymbol{G}$, where $\boldsymbol{R} = \boldsymbol{R}(\boldsymbol{x},\boldsymbol{y})$ is a regular function and $\boldsymbol{G} = \boldsymbol{G}(r)$ is the Green function of the problem, with $r = \|\boldsymbol{x}-\boldsymbol{y}\|_2$, containing a weak singularity $O(1/r)$. Then, Eq. (58) can be transformed by using two simplex coordinate sets, i.e. (ξ_1,ξ_2) over the element p and (η_1,η_2) over the element q (Fig. 15):

$$
\begin{aligned}
(\xi_1,\xi_2) &: 0 \leq \xi_1 \leq 1 \; ; \; 0 \leq \xi_2 \leq \xi_1 \\
(\eta_1,\eta_2) &: 0 \leq \eta_1 \leq 1 \; ; \; 0 \leq \eta_2 \leq \eta_1
\end{aligned} \qquad (59)
$$

The generic points on each of these triangles are transformed to elements p and q using

$$
\begin{aligned}
\boldsymbol{x}(\xi_1,\xi_2) &= \boldsymbol{N}^{(p)}(\xi_1,\xi_2)\boldsymbol{x}^{(p)} \\
\boldsymbol{y}(\eta_1,\eta_2) &= \boldsymbol{N}^{(q)}(\eta_1,\eta_2)\boldsymbol{x}^{(q)}
\end{aligned} \qquad (60)
$$

with the element shape functions

$$
\begin{aligned}
\boldsymbol{N}^{(p)}(\xi_1,\xi_2) &= \left[(1-\xi_1) \; (\xi_1-\xi_2) \; \xi_2\right] \\
\boldsymbol{N}^{(q)}(\eta_1,\eta_2) &= \left[(1-\eta_1) \; (\eta_1-\eta_2) \; \eta_2\right]
\end{aligned} \qquad (61)
$$

and the element nodal coordinates at the triangle vertices

$$
\boldsymbol{x}^{(p)} = \begin{bmatrix} \boldsymbol{x}_i \\ \boldsymbol{x}_j \\ \boldsymbol{x}_k \end{bmatrix} \quad ; \quad \boldsymbol{x}^{(q)} = \begin{bmatrix} \boldsymbol{x}_r \\ \boldsymbol{x}_s \\ \boldsymbol{x}_t \end{bmatrix} \qquad (62)
$$

Then, Eq. (58) is written as

$$\boldsymbol{Z} = \int_{A^{(p)}} \int_{A^{(q)}} \boldsymbol{L}(\boldsymbol{x},\boldsymbol{y}) \, \mathrm{d}A_{\boldsymbol{y}} \, \mathrm{d}A_{\boldsymbol{x}} = J^{(p)}J^{(q)} \, \tilde{\boldsymbol{L}} \qquad (63)$$

where $J^{(p),(q)} = 2A^{(p),(q)}$ are the Jacobians of each element, and $A^{(p),(q)}$ are their areas, respectively, whereas $\tilde{\boldsymbol{L}}$ is written in simplex coordinates as

$$\tilde{\boldsymbol{L}} = \int_0^1 \int_0^{\xi_1} \int_0^1 \int_0^{\eta_1} \boldsymbol{L}(\boldsymbol{\xi},\boldsymbol{\eta}) \, \mathrm{d}\eta_2 \, \mathrm{d}\eta_1 \, \mathrm{d}\xi_2 \, \mathrm{d}\xi_1 \qquad (64)$$

If the pairs of elements p and q are not contiguous nor coincidents, the kernel of Eq. (64) is regular and a Gauss–Legendre quadrature can be employed. When the pairs have a common edge or a common vertex, then edge or vertex weak singularities appear. If the pairs have both facets coincident, the whole integration domain is weakly singular. A systematic way to calculate the double surface integrals with flat triangular elements was given in [31], and extended in [43], based on a convenient reordering of the four iterate integrations that moves the weak singularity to the origin by using the Duffy transformations [31], i.e. the procedure regularizes the integrand by using polar coordinates. Then, a Gauss–Legendre numerical quadrature is used on the four coordinates. Further details can be found in [31, 35, 43, 44].